Does the HCN/CO ratio trace the star-forming fraction of gas? I. A comparison with analytical models of star formation

Bemis, A.R.; Wilson, C.D

Does the HCN/CO Ratio Trace the Star-forming Fraction of Gas? I. A Comparison with Analytical Models of Star Formation

Ashley R. Bemis[1,2] and Christine D. Wilson[2]

[1] Leiden Observatory, Leiden University, PO Box 9513, 2300 RA Leiden, The Netherlands; bemis@strw.leidenuniv.nl
[2] McMaster University, 1280 Main St W, Hamilton ON L8S 4M1, Canada

Abstract

We use archival ALMA observations of the HCN and CO $J = 1$–0 transitions, in addition to the radio continuum at 93 GHz, to assess the relation between dense gas, star formation, and gas dynamics in 10 nearby (ultra)luminous IR galaxies (U)LIRGs and late-type galaxy centers. We frame our results in the context of turbulent and gravoturbulent models of star formation to assess whether the HCN/CO ratio tracks the gravitationally bound star-forming gas in molecular clouds (f_{grav}) at subkiloparsec scales in nearby galaxies. We confirm that the HCN/CO ratio is a tracer of gas above $n_{\mathrm{SF}} \approx 10^{4.5}$ cm^{-3}, but the subkiloparsec variations in HCN/CO do not universally track f_{grav}. We find strong evidence for the use of varying star formation density-threshold models, which are able to reproduce trends observed in t_{dep} and ϵ_{ff} that fixed-threshold models do not reproduce. Composite lognormal and power-law models outperform pure lognormal models in reproducing the observed trends, even when a fixed power-law slope is used. The ability of the composite models to better reproduce the star formation properties of the gas provides additional indirect evidence that the star formation efficiency per freefall time is proportional to the fraction of gravitationally bound gas.

1. Introduction

A current challenge for understanding star formation in molecular clouds is determining the fraction of gas that is converted into stars over the lifetime of a cloud. Observations show that star formation sites primarily lie in regions of dense molecular gas in Milky Way clouds (Lada et al. 1991a, 1991b; Helfer & Blitz 1997a, 1997b), and these regions are confined to ~0.1 pc scales within larger molecular structures in the form of clumps or filaments (André et al. 2016). Within these gas structures, the fraction of gravitationally bound gas continues to form stars. Analytical models of star formation rely on estimates of the self-gravitating gas fraction, f_{grav}, to then predict the star formation rate (SFR; e.g., Krumholz & McKee 2005; Hennebelle & Chabrier 2011; Padoan & Nordlund 2011; Federrath & Klessen 2012; Burkhart & Mocz 2019), which makes f_{grav} an important parameter to constrain observationally.

Extragalactic observations rely on molecular transitions with high critical densities, $n_{\mathrm{crit}} \gtrsim 10^4$ cm^{-3}, to gain information on the dense gas in other galaxies. The most commonly used dense molecular gas tracer in extragalactic studies is the HCN $J = 1$–0 transition (Gao & Solomon 2004a, 2004b). Under the common assumption that the total emissivity of HCN traces the dense gas mass, $I_{\mathrm{HCN}} \propto \Sigma_{\mathrm{dense}}$, the ratio of the HCN and CO emissivities, $I_{\mathrm{HCN}}/I_{\mathrm{CO}}$, is proportional to the fraction of molecular gas in the dense phase, f_{dense}. If the dense gas mass traced by HCN

is also self-gravitating, then this line ratio is a simple observational method for estimating f_{grav}. However, the interstellar medium (ISM) of galaxies resides at a range of densities $\lesssim 1 - \gg 10^8$ cm^{-3}, and molecular transitions are sensitive to a continuum of these densities, including some fraction below their critical density (Shirley 2015; Leroy et al. 2017a). Recent studies within the Milky Way have also shown that HCN may predominantly trace moderate gas densities (Kauffmann et al. 2017), rather than denser gas associated with star formation. The fraction of CO-dark or CO-faint gas may also contribute to variations in $I_{\mathrm{HCN}}/I_{\mathrm{CO}}$ (Grenier et al. 2005; Wolfire et al. 2010; Bolatto et al. 2013). On average in the Milky Way, ~30% of molecular hydrogen appears to be CO-faint (Pineda et al. 2013; Langer et al. 2014). This fraction is higher in lower-metallicity gas (Pineda et al. 2013; Jameson et al. 2018; Chevance et al. 2020) and appears to be more significant for clouds at lower masses (Grenier et al. 2005; Bolatto et al. 2013) and at higher radii in the Milky Way (Pineda et al. 2013; Langer et al. 2014; Chevance et al. 2020). This would likely result in over-estimates of f_{dense} in lower-mass clouds, assuming HCN emission is not affected in the same way. This is likely less significant in more extreme systems (e.g., luminous IR galaxies, LIRGs, or ultraluminous IR galaxies, ULIRGs) or galaxy centers, such as those studied in this paper.

The dynamics of the gas in the ISM are set by a combination of gravity, turbulence, and magnetic fields, and these processes act together to set the spatial structure of gas in ISM clouds. These processes also likely play a role in setting the star formation properties of the ISM. One type of analytical model, gravoturbulent models of star formation, aims to predict both the observed structure of gas clouds and their star formation properties. In particular, gravoturbulent models of star formation predict the shape of the gas volume

density probability distribution function ($n - \mathrm{PDF}$) and the star formation efficiency (ϵ_{ff}) over a freefall time (t_{ff})[3] (Krumholz & McKee 2005; Hennebelle & Chabrier 2011; Padoan & Nordlund 2011; Federrath & Klessen 2012; Imara & Burkhart 2016; Burkhart 2018).[4] Studies have found that the column density PDF of the diffuse ($n < 1$ cm^{-3}) component of gas in the Milky Way and M33 is consistent with a lognormal PDF (see Berkhuijsen & Fletcher 2008; Hill et al. 2008; Tabatabaei et al. 2008; Burkhart et al. 2015). The seminal analytical work by Vazquez-Semadeni (1994) showed that if the turbulent ISM develops a series of isothermal and interacting supersonic shocks, the gas would naturally follow a lognormal PDF (see Vazquez-Semadeni 1994; Padoan et al. 1997; Scalo et al. 1998; Nordlund & Padoan 1999.) In this picture, the shocks amplify each other via a turbulent cascade of energy, and this multiplicative process causes the gas density PDF to assume a lognormal shape (see Vazquez-Semadeni 1994; Padoan et al. 1997; Scalo et al. 1998; Nordlund & Padoan 1999; Chen et al. 2018).

Observations of molecular regions of the ISM reveal that the gas column density PDF takes on a different form at high densities. The highest-density regions within more evolved molecular clouds contribute a power-law tail to the gas column density PDF (see Chen et al. 2018), with some cloud PDFs being almost entirely power law (e.g., Kainulainen et al. 2009; Schneider et al. 2013; Lombardi et al. 2015; Schneider et al. 2015, 2016; Alves et al. 2017). This power law has also been observed in simulations that develop self-gravitating gas (see Ballesteros-Paredes et al. 2011; Collins et al. 2012; Schneider et al. 2015; Burkhart et al. 2017; Padoan et al. 2017.) These results strongly suggest that the gas density PDF in a star-forming molecular cloud is likely a combination of a lognormal and power-law shape, and that the power-law tail is potentially the result of gas becoming self-gravitating. The fraction of gas within this power-law tail would then be the self-gravitating gas fraction, f_{grav}. The density at which the $n - \mathrm{PDF}$ transitions from a lognormal to power-law shape would then represent the moment at which gas becomes available to star formation, n_{SF}. The fraction of dense gas mass above n_{SF} (f_{grav}) relative to the total mass of a star-forming cloud is then

$$f_{grav} = \frac{M(n > n_{SF})}{M}. \tag{1}$$

Turbulent models of star formation estimate ϵ_{ff} by integrating over a purely lognormal gas density PDF, also above a gas threshold density (see Krumholz & McKee 2005; Hennebelle & Chabrier 2011; Padoan & Nordlund 2011; Federrath & Klessen 2012). This threshold density is also meant to capture the point at which gas becomes self-gravitating in the ISM, so that the fraction of gas above this threshold is f_{grav} in these models. However, lognormal-only models fail to explain observed variations in ϵ_{ff} and Mach number, $\mathcal{M}$, seen in some galaxies (e.g., Leroy et al. 2017b). For example, giant molecular clouds (GMCs) in M51 show a weak anticorrelation between velocity dispersion (which is proportional to $\mathcal{M}$; see

Equation (11)) and the star formation efficiency of gas per freefall time, ϵ_{ff}.[5] Leroy et al. (2017a) argue that this anticorrelation may reflect differences in the dynamical state of their clouds with galactocentric radius.

Burkhart & Mocz (2019) show that including a power-law tail in the gas volume density PDF reproduces the observed variations in ϵ_{ff} in M51, without requiring changes in the dynamical state of the clouds and without explicitly setting n_{SF}. They find a slight anticorrelation between ϵ_{ff} and $\mathcal{M}$ for virialized clouds ($\alpha_{vir} \approx 1$). This anticorrelation coincides with an increasing depletion time with $\mathcal{M}$, in agreement with the findings from PAWS (Leroy et al. 2017b). $\epsilon_{ff} \propto f_{grav}$ implies f_{grav} may also anticorrelate with $\mathcal{M}$. Thus, without needing to explicitly set n_{SF}, it is ultimately a decrease in f_{grav} with respect to increasing $\mathcal{M}$ that leads to the anticorrelation between σ_{rv} and ϵ_{ff} (Burkhart & Mocz 2019). However, in starbursts where $\mathcal{M}$ is higher, we see higher ϵ_{ff} and shorter t_{dep} on average (Wilson et al. 2019). Starbursts typically have enhanced HCN/CO ratios in addition to a shorter depletion time t_{dep} (Kennicutt & De Los Reyes 2021). If $I_{HCN}/I_{CO} \propto f_{dense}$ and $f_{dense} \propto f_{grav}$, then the result from BM19 appears to differ from what is observed in starbursts.

A potential explanation for these differences may be differences in the timescale for star formation, which may be set by the environment in which a gas cloud is immersed. The star formation law can be written as (Krumholz et al. 2012)

$$t_{ff} \Sigma_{SFR} = \epsilon_{ff} \Sigma_{gas}, \tag{2}$$

where Σ_{gas} is the gas surface density, Σ_{SFR} is the SFR surface density, and t_{ff} is the freefall time and is set by the self-gravity of a cloud.

Burkhart & Mocz (2019) demonstrate the connection between f_{grav} and the instantaneous efficiency of the gas, $\epsilon_{inst} \approx \epsilon_0 f_{grav}$, which reflects both the local efficiency, ϵ_0 (set, e.g., by stellar feedback), and f_{grav}. This local efficiency may correlate with its observational analog, the star formation efficiency per freefall time, ϵ_{ff} (Krumholz & McKee 2005; Lee et al. 2016). Furthermore, if turbulence plays a significant role in setting n_{SF}, then we may find a correlation between ϵ_{ff}, observed velocity dispersions of gas, and turbulent pressure. Turbulent models of the ISM predict a dependence of σ_{n/n_0}, the density variance of the volume density PDF ($n - \mathrm{PDF}$) on the sonic Mach number, $\mathcal{M} = \sigma_{v,3D}/c_s$,[6] within individual star-forming clouds. Lada et al. (1994) found a correlation between the extinction, A_V, in the dark cloud IC 5126 and the standard deviation of A_V, with extinction increasing with dispersion (Goodman et al. 2009). Kainulainen & Tan (2013) find a correlation between measurements of the velocity dispersion from ^{12}CO and ^{13}CO and the density contrast (N/N_0) of the column density PDFs ($N - \mathrm{PDFs}$) derived from IR data in several Milky Way clouds. Combined, these correlations imply that the CO velocity dispersion may be sensitive to the density variance of $N - \mathrm{PDF}$, σ_{N/N_0} (where $\sigma_{N/N_0} \propto \ln(N/N_0)$), and therefore is a probe of the ISM physics.

In external galaxies where resolution is limited, molecular line ratios are an additional tool for assessing the $n - \mathrm{PDF}$

---

[3] Brunt et al. (2010) find that the two-dimensional column density distribution is a compressed version of the three-dimensional (volume) density distribution. Burkhart & Lazarian (2012) provide an analytical framework for connecting these two distributions when both contain lognormal components, which we adopt in this paper.

[4] Freefall time is treated differently depending on the framework used, and in reality, it must be a reflection of multiple freefall times from the array of gas densities that span the $n - \mathrm{PDF}$.

[5] We briefly discuss the observational uncertainties associated with estimates of $\mathcal{M}$, which depend on measurements of velocity dispersion, in Section 2.5.

[6] The sound speed is given by $c_s = \sqrt{kT_{kin}/\mu m_H}$, T_{kin} is the gas kinetic temperature, $\mu = 2.33$ (Kauffmann et al. 2008) is the mean molecular weight, and m_H is the Hydrogen mass. $\sigma_{v,3D}$ is the three-dimensional velocity dispersion and is related to the one-dimensional velocity dispersion via $\sigma_{3D,v} = \sqrt{3}\,\sigma_v$.

Table 1
Spatial and Spectral Resolutions of the Data for Each Galaxy

Galaxy	Beam (″)	Distance[a] (Mpc)	Scale (pc beam^{-1})	δv (km s^{-1})	i[b] (°)	z	AGN	Bar	Interacting	Classification
M83	2.10	4.7	48	10	24	0.00171	⋯	Y	⋯	SB
Circinus	3.00	4.2	61	20	66	0.00145	Sy 2	⋯	⋯	SB
NGC 3351	3.45	9.3	156	10	45.1	0.00260	⋯	Y	N	SB
NGC 3627	4.15	9.4	189	20	56.5	0.00243	LINER/Sy 2	Y	Y	Post-SB
NGC 1808	3.75	7.8	142	10	57	0.00322	Sy 2	Y	⋯	SB
NGC 7469	0.95	66.4	306	20	45	0.01632	Sy 1	⋯	Y	LIRG
NGC 3256	2.20	44	469	27.5	⋯	0.00935	South Nucleus	N	Y	LIRG
NGC 4038	5.00	22	110	5.2	⋯	0.00569	⋯	N	Y	SB
IRAS 13120-5453	1.10	134	715	20	⋯	0.02076	Sy 2	N	⋯	ULIRG
VV114	2.30	81	903	20	⋯	0.02007	East Nucleus	N	Y	LIRG

Notes.
[a] Distances from Wilson et al. (2023).
[b] M83: Tilanus & Allen (1993); Circinus: Jarrett et al. (2003); NGC 3351 & NGC 3627: Sun et al. (2020); NGC 1808: Salak et al. (2019).
[c] Distances and redshifts are also listed. They are used to determine the physical scale (in pc) per pixel, and to convert measured flux into luminosities. Redshifts are taken from the NASA/IPAC Extragalactic Database (NED). Inclination angles are taken from the papers listed below the table. Distances are the same as in Wilson et al. (2023), except for NGC 3627. We use the distance for NGC 3627 taken from Jiménez-Donaire et al. (2019) for consistency when comparing with the EMPIRE data. We also list the presence or absence of an AGN, bar, or interaction with another galaxy. These classifications are taken from the NED.

shape. Shirley (2015) showed that molecular transitions have an emissivity[7] that extends over a range of gas densities, including a significant amount of emission at densities below the critical density associated with that transition.[8] To determine whether molecular line ratios remain sensitive to $n-$PDF shape, Leroy et al. (2017a) modeled molecular line emissivities and explored a range of $n-$PDF shapes. They reported that dense gas tracers (e.g., HCN and HCO$^+$) are more sensitive to changes in the shape of the $n-$PDF than lower-density tracers such as CO. Combining molecular line ratios of dense gas tracers with information on kinematics is therefore a promising tool for assessing the $n-$PDF information of clouds in external galaxies.

To assess the relation between the HCN/CO ratio and f_{grav}, we examine more extreme star-forming environments in which turbulence is stronger (e.g., mergers, starbursts, (U)LIRGs, or barred galaxies). We study a sample of 10 (U)LIRGs and disk galaxy centers that have archival CO, HCN, CN, and HCO$^+$ $J=1-0$ data, in addition to 93 GHz radio continuum. In this paper, we focus on general trends of the HCN/CO ratio, the SFR surface density, and ϵ_{ff}, and we compare these modeled trends with the observed trends in our sample. We use the EMPIRE sample of galaxies (Jiménez-Donaire et al. 2019) as a comparison, which predominantly targets normal regions of star formation within galaxy disks.

2. Data and Sample

Our sample consists of 10 nearby ($z < 0.03$) galaxies, including the dense centers of five disk galaxies and five mergers and (U)LIRGs. We list these galaxies and their basic properties in Table 1. Four of the five disk galaxies in our sample are also barred. For each galaxy, we image archival ALMA data of the HCN, CN, CO, and HCO$^+$ $J=1-0$ transitions, in addition to the radio continuum emission at

93 GHz. The data are uv-matched and tapered to a common beam for each individual galaxy. The sample selection and data reduction process are presented in Wilson et al. (2023) in detail, except for NGC 4038/9, NGC 1808, and NGC 3351, which have been reduced and imaged separately at higher velocity resolutions to be included in this analysis.

2.1. Moment Maps

We produce maps of the integrated intensity and velocity dispersion of the CO and HCN $J=1-0$ transitions using the Astropy Spectral Cube package (Ginsburg et al. 2019). We implement a masking method similar to that in Sun et al. (2018) and summarize the masking method here:

1. The r.m.s. noise is estimated in each channel of each datacube using the median absolute standard deviation.
2. Peaks of emission with a signal-to-noise ratio (S/N) of at least 5 across two channels are identified within each datacube.
3. Masks are expanded around these peaks down to channels with emission at an S/N of 3.
4. Emission from regions smaller than a beam area are masked.

We calculate the uncertainty in integrated intensity and velocity dispersion using Equations (A2) and (A6), respectively. We require that all pixels have S/N > 3 in integrated intensity in addition to an S/N > 2 in velocity dispersion.

2.2. Molecular Gas Surface Densities

One of the main goals of this study is to assess variations in the fraction of gas in the dense phase as traced by the HCN and CO molecular line luminosities. Our analysis allows us to estimate trends in the HCN and CO luminosity-to-mass conversion factors (see Bolatto et al. 2013), which we define as

$$\alpha_{mol} = \frac{\Sigma_{mol}}{I_{mol}} \qquad [M_\odot \text{ pc}^2 \text{ (K km s}^{-1})^{-1}], \qquad (3)$$

where Σ_{mol} is the mass surface density of the molecular gas, including helium, $I_{mol} = L_{mol}/A_{pix}$ is the intensity in units of K

---

[7] Emissivity, which describes the emission per mass surface density, is effectively the inverse of a molecular line conversion factor.
[8] Here the critical density is the density at which collisional interactions balance instantaneous deexcitation of a particular molecular transition (Draine 2011).

km s^{-1}, and L_{mol} is total luminosity over the physical area of a pixel, A_{pix}. To calculate the molecular gas mass surface density, Σ_{mol}, we use

$$\Sigma_{mol} = \alpha_{mol} \, I_{mol} \, \cos(i). \qquad (4)$$

We apply inclination angles only to the disk galaxies in this sample, as inclination angles are typically uncertain in mergers and (U)LIRGs. Thus, the uncorrected measurements of galaxies with nonzero inclinations will result in overestimates of Σ_{mol} and other surface densities.

To facilitate comparison with other studies, our fiducial value is $\alpha_{CO} = 1.1$ [$M_\odot$ (K km s^{-1} pc^2)$^{-1}$] for our sample of galaxies, the (U)LIRG value including helium (Downes et al. 1993), which is about four times lower than the Milky Way value. This lower value is motivated by evidence that gas in these systems is subject to more extreme excitation mechanisms, e.g., higher temperatures and densities (see Downes et al. 1993; Bolatto et al. 2013 and references therein). Additionally, the gas traced by CO in these systems often shows broad line widths, potentially reducing the opacity of the CO transition (Downes et al. 1993; Bolatto et al. 2013). Downes et al. (1993) also suggest that CO may be subthermally excited ($T_{ex} < T_{kin}$) in starbursts and (U)LIRGs. We choose a fixed value of $\alpha_{CO} = 4.35$ [$M_\odot$ (K km s^{-1} pc^2)$^{-1}$] for the EMPIRE sample of galaxies because these are mostly disk galaxies and are likely more similar to the Milky Way than to starbursts. Because we already have NGC 3627 in our sample, we drop NGC 3627 from the EMPIRE data.

The HCN conversion factor is less certain. Historically, $\alpha_{HCN} \approx 13.6$ [$M_\odot$ (K km s^{-1} pc^2)$^{-1}$] has been used (Gao & Solomon 2004a, 2004b), which is appropriate for a virialized cloud core with a mean density $n_{H_2} \sim 3 \times 10^4$ cm^{-3} and brightness temperature $T_B \sim 35$ K (e.g., Radford et al. 1991, including helium). This HCN conversion factor assumes that this molecular transition is optically thick and that the gas it traces is in local thermodynamic equilibrium (LTE). In Bemis (2020) and Bemis & Wilson (in prep.), we explore variations in the relative values of α_{HCN} and α_{CO} using an nonLTE radiative transfer analysis. If all of the above assumptions are true, then the fraction of dense gas traced by HCN/CO is given by

$$f_{dense} = \frac{\alpha_{HCN}}{\alpha_{CO}} \frac{I_{HCN}}{I_{CO}}, \qquad (5)$$

with $\alpha_{HCN}/\alpha_{CO} = 3.2$ implied from the above discussion. We do this assuming that the physical effects impacting α_{CO} will impact α_{HCN} in a similar way. Simulations show that a slight reduction in α_{HCN} does happens in presence of higher gas temperatures ($T_{kin} = 20$ K; see Onus et al. 2018), similar to our expectation for α_{CO}. Furthermore, by using $\alpha_{HCN}/\alpha_{CO} = 3.2$, our plots of f_{dense} are a direct reflection of the HCN/CO ratio. We distinguish this calculation of f_{dense} from analytical estimates of the fraction of dense star-forming gas, which is generally defined as the mass fraction above the density at which gas becomes self-gravitating, f_{grav}.

2.3. The Radio Continuum SFR

We detect radio continuum emission at 93 GHz in all of our sources and use this as our SFR tracer. The radio continuum is a combination of thermal (T) free–free emission and non-thermal (NT) synchrotron emission from regions with massive star formation, spanning $\sim$1–100 GHz. At 93 GHz, we are in the regime where thermal free–free emission from young star-forming regions will likely dominate the radio continuum emission. Nonthermal emission is expected to contribute $\sim$25% to the radio continuum luminosity at this frequency (see Murphy et al. 2011; Wilson et al. 2019), assuming an electron temperature $T_e \sim 10^4$ K and nonthermal spectral index $\alpha_{NT} \sim 0.84$. This fraction will change if there are variations in either T_e or α_{NT}. We adopt fixed values for $\alpha_{NT} = 0.84$ and $T_e = 10^4$ K, and we use the composite calibration from Murphy et al. (2011), which accounts for both thermal and nonthermal contributions to the SFR,

$$\left(\frac{SFR_\nu}{M_\odot \, yr^{-1}} \right)$$
$$= 10^{-27} \left[2.18 \left(\frac{T_e}{10^4 \, K} \right)^{0.45} \left(\frac{\nu}{GHz} \right)^{-0.1} \right.$$
$$\left. + 15.1 \left(\frac{\nu}{GHz} \right)^{-\alpha^{NT}} \right]^{-1} \left(\frac{L_\nu}{erg \, s^{-1} \, Hz^{-1}} \right). \qquad (6)$$

At 93 GHz, the radio continuum emission from star-forming regions may overlap with the lower-frequency tail of the dust SED. Wilson et al. (2019) estimate a $\sim$10% contribution from dust at 93 GHz for IRAS 13120-5453, NGC 3256, and NGC 7469, the three most IR-luminous galaxies in our sample. We adopt this correction factor of $\sim$10% for all sources, but we acknowledge that the emissivity of dust at 93 GHz may vary between our sources. We further mask pixels that may be contaminated with emission from an active galactic nucleus (AGN; see Table 1).

Variations in T_e and α_{NT} will impact our SFR estimates from the radio continuum at 93 GHz. Electron temperatures typical of HII regions are $T_e \sim 5 \times 10^3 - 10^4$ K, which will produce a change of $\sim$30% (Murphy et al. 2011). In contrast to this, α_{NT} has been observed as low as $\sim$0.5, which would also give a change in luminosity $\sim$30% at 93 GHz. Wilson et al. (2019) also find evidence of a significant fraction (up to 50%) of nonthermal emission in NGC 7469 at 93 GHz by comparing with an archival radio continuum map at 8 GHz. We adopt an uncertainty of 30% for SFR estimates derived from the radio continuum.

We compare the results of our sample with those of the EMPIRE survey (Jiménez-Donaire et al. 2019), for which there are publicly available single-dish (IRAM 30m) observations of HCN and CO. We estimate Σ_{SFR} in EMPIRE galaxies using 24 μm IR maps from the Spitzer Space Telescope. These IR data are convolved to a 15″ Gaussian beam using Aniano et al. (2011) Gaussian kernels and further smoothed to a 33″ Gaussian beam using CASA (McMullin et al. 2007). Backgrounds are subtracted and SFRs are derived using the Rieke et al. (2009) calibration.

2.3.1. Star Formation Timescales and Efficiency

We use the SFR and molecular gas surface densities to estimate the depletion time of the total (mol = CO) and dense (mol = HCN) molecular gas content,

$$t_{dep} = \frac{\Sigma_{mol}}{\Sigma_{SFR}}, \qquad (7)$$

where Σ_{mol} is estimated using Equation (4). To estimate the dimensionless star formation efficiency, we compare this depletion timescale with the freefall timescale,

$$t_{ff} = \sqrt{\frac{3\pi}{32G\rho}}, \qquad (8)$$

where ρ is a characteristic density of the gas associated with star formation. We calculate gas density assuming a fixed line-of-sight (LOS) depth via $\rho \approx \Sigma_{mol}/R$, where R is equivalent to half of the cloud or gas depth along the LOS. We do not know R, so we assume a fixed value of 100 pc for all galaxies when estimating ρ. We also explored estimating the freefall time using the Krumholz et al. (2012) prescriptions for t_{ff} in the GMC and Toomre regimes. We find little qualitative difference in the results between using t_{ff} as described above and the Krumholz et al. (2012) prescription.

The efficiency of the star formation process is then estimated by comparing the observed depletion timescales with estimates of the freefall time,

$$\epsilon_{ff} = \frac{t_{ff}}{t_{dep}}, \qquad (9)$$

which is just the star formation law (Equation (2)) rewritten in terms of depletion time.

2.4. Velocity Dispersion

We measure the one-dimensional velocity dispersion of the molecular gas in our sources, σ_v, using the CO $J = 1-0$ transition. The velocity dispersions, $\sigma_{v,meas}$, are measured directly from moment 2 maps. We correct for broadening of the line due to the finite spectral resolution of our data using Rosolowsky & Leroy (2006),

$$\sigma_v = \sqrt{\sigma_{v\,meas}^2 - \frac{\delta v^2}{2\pi}}, \qquad (10)$$

where δv is the channel resolution at which we image the data. This value is then converted into the three-dimensional velocity dispersion via $\sigma_{v,3D} = \sqrt{3}\,\sigma_v$.

2.4.1. Velocity Dispersion as a Tracer of Mach Number

As previous studies have done for Milky Way clouds (Kainulainen & Federrath 2017), we used CO line widths as an indicator of the Mach number of the gas in our galaxies,

$$\mathcal{M} = \frac{\sqrt{3}\,\sigma_{v,1D}}{c_s}, \qquad (11)$$

where c_s is the thermal sound speed, and $\sigma_{v,1D}$ is the observed one-dimensional velocity dispersion. There are limits to this approach, and the ability of the CO line to trace cloud turbulence may be limited by its optical depth (Goodman et al. 2009; Burkhart et al. 2013), and the observed line width can include disk rotation or other large-scale motions, but alternative measures of gas kinematics in extragalactic clouds are lacking.

To estimate c_s, we consider an ideal gas equation of state ($P_{th} = nk_BT/\mu m_H$), such that the sound speed is $c_s = \sqrt{k_BT/\mu m_H}$, where k_B, T, μ, and m_H are the Boltzmann constant, gas kinetic temperature, the mass of a hydrogen atom,

and the mean particle weight. For a gas in which hydrogen is primarily in molecular form, $\mu = 2.33$ (assuming cosmic abundances; Kauffmann et al. 2008). For $\mu = 2.33$ and a temperature range of $T = 10$–100 K, $c_s \approx 0.2$–0.6 km s^{-1}. The choice of c_s can have a significant impact on the estimate of $\mathcal{M}$. We choose an intermediate value $c_s = 0.4$ km s^{-1}, corresponding to $T \sim 45$ K, as our fiducial value.

2.5. Uncertainties from a Multiscale Sample

The spatial resolution of the data in our sample spans ~ 50–900 pc. We consider how this range may impact our measurements from the context of a turbulent ISM, and how we can best interpret the measured σ_v and line ratios in our sources. The beam-filling fraction, $\phi_{ff,beam}$ is less of an uncertainty in this study because the sources with the lowest resolution are (U)LIRGs and likely have filling fractions approaching unity, while the spiral galaxy centers have resolutions approaching cloud scales. This reduces the issue of variations in the beam-filling fractions from galaxy to galaxy. A significant source of uncertainty instead comes from variations in the relative filling fractions of the HCN/CO transitions,

$$\Phi_{HCN/CO} \approx \frac{r_{HCN}^2}{r_{CO}^2}, \qquad (12)$$

where r_{HCN} and r_{CO} are the average radial extents of HCN and CO, respectively. We explore variations in the filling fraction in Bemis (2020) and Bemis & Wilson (in prep.) from a radiative transfer perspective.

In addition to the uncertainty in $\Phi_{HCN/CO}$, the velocity dispersion in a turbulent medium is scale dependent (ℓ) such that (Larson 1981; Heyer et al. 2009)

$$\sigma_v(\ell) = \sigma_{v,L}\left(\frac{\ell}{L}\right)^p, \qquad (13)$$

where $p \sim 0.33$–0.5 depends on the type of turbulence (e.g., $p \approx 0.33$ for Kolmogorov, Larson 1981), L can be defined as the cloud diameter (or turbulent injection scale), and $\sigma_{v,L}$ is the cloud dispersion at that scale. A sample of galaxies at different physical scales will therefore be affected by this scale dependence, such that velocity dispersions will be lower at smaller scales and vice versa. However, this relation should saturate at the turbulent injection scale, which may mitigate some of this uncertainty. If larger-scale cloud-cloud motions do not affect the velocity dispersions of CO, then this saturation should be detected, although there is still an uncertainty in L. This means that lower-resolution observations may still be useful for assessing σ_v.

3. Model Framework: Gravoturbulent Models of Star Formation

We consider several prescriptions of f_{grav} in the context of analytical models of star formation and compare the predictions of these models to measurements of the I_{HCN}/I_{CO} ratio and the star formation properties of our galaxies. We use Equation (2), which is relevant to gravoturbulent models of star formation (KMD12).

ϵ_{ff} is calculated by integrating over the star-forming portion of the density-weighted gas density PDF (e.g., Krumholz & McKee 2005; Hennebelle & Chabrier 2011;

Padoan & Nordlund 2011; Federrath & Klessen 2012),

$$\epsilon_{\rm ff} = \epsilon_0 \int_{n_{\rm SF}}^{\infty} \frac{t_{\rm ff}(n_0)}{t_{\rm ff}(n)} \frac{n}{n_0} p(n) {\rm d}n. \qquad (14)$$

Here $p(n)$ is the volumetric density PDF of the cloud, $n - {\rm PDF}$, and n_0 is its mean density. The $n - {\rm PDF}$ characterizes the distribution of densities of the entire gas within the cloud, including the diffuse atomic and molecular components. We briefly review specific terms within this equation individually.

$p(n)$: Isothermal gas in the presence of supersonic turbulence naturally becomes distributed such that its $n - {\rm PDF}$ is roughly lognormal (Vazquez-Semadeni 1994; Nordlund & Padoan 1999; Wada & Norman 2001). Earlier formalisms of gravoturbulent models adopt a purely lognormal form of $p(n)$ (e.g., Krumholz & McKee 2005; Padoan & Nordlund 2011; Federrath & Klessen 2012). In terms of the logarithmic volume density $s = \ln(n/n_0)$, this is given by

$$p_s = N \frac{1}{\sqrt{2\pi\sigma_s^2}} \exp\left(-\frac{(s-s_0)^2}{2\sigma_s^2}\right), \qquad (15)$$

where N is a normalization constant,[9] σ_s^2 is the logarithmic density variance, which depends on the underlying physics of the gas and sets the width of $p(n)$, and $s_0 = -0.5\,\sigma_s^2$. Newer formalisms (i.e., Burkhart 2018) of gravoturbulent models of star formation suggest that the $n - {\rm PDF}$ may then evolve to include a high-density power-law tail that contains gas that is becoming gravitationally unstable to collapse. Observations of clouds in the Milky Way support a composite form of $p(n)$, where a power-law tail is clearly present in addition to a more diffuse component of gas. Burkhart (2018) presents this as a piecewise function,

$$p_s = \begin{cases} N\frac{1}{\sqrt{2\pi\sigma_s^2}}\exp\left(-\frac{(s-s_0)^2}{2\sigma_s^2}\right), & s < s_t \\ NCe^{-\alpha_{\rm PL}s}, & s > s_t \end{cases} \qquad (16)$$

where s_t is the logarithmic form of the transition density between the two components of the $n - {\rm PDF}$, and $\alpha_{\rm PL}$ is the slope of the power-law tail. The factors N and C are normalization constants given by Burkhart (2018).

σ_s: Numerical studies have shown that if the turbulence is super-Alfvénic and the magnetic field (B) follows a power-law relation with gas density, $B \propto n^{1/2}$, then the logarithmic density variance is given by (Molina et al. 2012; Federrath & Klessen 2012)

$$\sigma_s^2 = \ln\left(1 + b^2\mathcal{M}^2\frac{\beta}{\beta+1}\right), \qquad (17)$$

where $\mathcal{M}$ is the Mach number, $\beta = P_{\rm th}/P_{\rm mag}$ is the plasma beta (which characterizes the ratio of thermal pressure to magnetic pressure), and b is the turbulent forcing parameter (which characterizes the relative amount of solenoidal $b = 1$ or compressive $b = 0.33$ turbulence within the gas). Without a clear prescription for β and b in our sample, we simply take $\beta \to \infty$, which assumes that $B = 0$ G. We take an intermediate value $b = 0.4$, which assumes that turbulence is a mixture of compressive and solenoidal forcing. Nonisothermal gas will

---

add intermittency, resulting in deviations from a lognormal shape of $p(n)$ (Federrath & Banerjee 2015). For the purpose of this work, we assume that an underlying lognormal is a reasonable intermediate approximation to part of the $n - {\rm PDF}$ (Federrath & Banerjee 2015).

$n_{\rm SF}$: Gravity overcomes supportive processes and begins the process of collapse above the density threshold, $n_{\rm SF}$. The processes competing with gravity include some combination of magnetic support, internal turbulent motions, and external ISM pressures. Any gas with densities higher than $n_{\rm SF}$ is then potentially gravitationally unstable and star forming, so that $n_{\rm SF}$ serves as the lower limit of the integration that determines $\epsilon_{\rm ff}$.

$t_{\rm ff}(n_0)/t_{\rm ff}(n)$: Within the integral in Equation (14), the integral is a freefall time factor, which converts the integrand into a dimensionless mass rate equivalent to the mass per freefall time (Federrath & Klessen 2012). This time factor is treated differently depending on the analytical model being considered, e.g., single-freefall (SFF) time (Krumholz & McKee 2005; Padoan & Nordlund 2011) versus multi-freefall (MFF) time models (Hennebelle & Chabrier 2011; Federrath & Klessen 2012), and these differences are summarized in Federrath & Klessen (2012) and Burkhart (2018). MFF models keep this factor in the integral, which predicts different rates of collapse for different densities, while SFF models take this factor out of the integral. Due to this difference, MFF models predict higher $\epsilon_{\rm ff}$.

ϵ_0: The prefactor in Equation (14), ϵ_0, is the local dimensionless efficiency of star formation. ϵ_0 depends on additional processes, such as the level of stellar feedback dispelling some of the gas that is already above $n_{\rm SF}$ (Burkhart & Mocz 2019). The mass that is converted into stars is then $M_* = \epsilon_0 M(n > n_{\rm SF})$.

3.1. Different Formalisms of Gravoturbulent Models of Star Formation

Federrath & Klessen (2012) and Burkhart (2018) both provide analytical equations for estimating $\epsilon_{\rm ff}$ for different gravoturbulent formalisms that we adopt in this analysis. In this work, we focus on three analytical models that each have unique prescriptions for the density threshold and the shape of the $n - {\rm PDF}$: 1. the Padoan & Nordlund (2011) formalism, 2. the Burkhart (2018) and Burkhart & Mocz (2019) formalism, and 3. a fixed density-threshold model, which is not explicitly formulated in previous works, but is often referenced in the literature when interpreting the results of studies using dense gas tracers (e.g., Gao & Solomon 2004a, 2004b).

We mainly refer to analytical equations from Burkhart (2018) for brevity, but also refer to Federrath & Klessen (2012) for another comprehensive summary of analytical models, as well as to the original papers that have provided the basis of this work, e.g., Krumholz & McKee (2005), Padoan & Nordlund (2011), and Hennebelle & Chabrier (2011). We summarize the following important quantities of each of the models we use in this work: (a) the underlying $n - {\rm PDF}$ shape of the model, $p(n)$, (b) the equation used to estimate $\epsilon_{\rm ff}$, (c) the star formation threshold density, $n_{\rm SF}$, and (d) the method we use to determine $f_{\rm grav}$.

  1. The Padoan & Nordlund (2011) formalism:
    (a) These models have a lognormal (LN) $n - {\rm PDF}$ (see Equation (15)).

(b) Padoan & Nordlund (2011) estimate ϵ_{ff} using (see Equation (13) in Burkhart 2018)

$$\epsilon_{ff,PN11} = \frac{\epsilon_0}{2}\left\{1 + \text{erf}\left(\frac{\sigma_s^2 - 2\,s_{thresh}}{\sqrt{8}\,\sigma_s}\right)\right\} \times \exp\left(s_{thresh}/2\right), \quad (18)$$

where $s_{thresh} = \exp(n_{SF}/n_0)$.[10]

(c) The Padoan & Nordlund (2011) equation for n_{SF} that determines s_{thresh} in Equation (18) is given by (see Equation (11) in Burkhart 2018)

$$n_{SF} \approx 0.54\, n_0\, \alpha_{vir}\, \mathcal{M}^2, \quad (19)$$

where we have taken the prefactor in their original equation to be $\phi = 0.35$ and have neglected magnetic fields. The remaining dependence is then only on mean density, virial parameter (α_{vir}), and $\mathcal{M}$.[11] We can also rewrite this equation in terms of the turbulent pressure, which we are able to estimate directly from our data (see Walker et al. 2018),

$$n_{SF} \approx 0.36\, \alpha_{vir}\, \frac{P_{turb}}{k_B\, T_{kin}}, \quad (20)$$

where $P_{turb} \approx (3/2)\Sigma_{mol}\sigma_v^2/R$ or $P_{turb} \approx (3/2)n_0\sigma_v^2$ for the data and models, respectively. The direct scalings $n_{SF} \propto \mathcal{M}^2$ and $n_{SF} \propto P_{turb}$ assume that turbulence acts as a supportive process to the gas. The virial parameter, α_{vir}, is given by

$$\alpha_{vir} \approx \frac{5\sigma_v^2 R}{G\Sigma}, \quad (21)$$

and it is the ratio of internal kinetic to gravitational energy in a cloud, E_{kin} and E_{grav}.

(d) For these models, we perform a numerical integration of the $n - PDF$ above n_{SF} (Equation (19)) to calculate f_{grav}.[12]

2. The Burkhart (2018) and Burkhart & Mocz (2019) formalism:

(a) These models have a piecewise (lognormal plus power law, LN+PL) $n - PDF$ (see Equation (16)).

(b) (Burkhart 2018) calculate ϵ_{ff} using a composite LN+PL $n - PDF$ (see Equation (27) in Burkhart 2018),

$$\epsilon_{ff,BM18}$$
$$= N \exp\left(s_{thresh}/2\right)\frac{\epsilon_0}{2}\left\{\text{erf}\left(\frac{\sigma_s^2 - 2\,s_{thresh}}{\sqrt{8}\,\sigma_s}\right)\right.$$
$$\left. - \text{erf}\left(\frac{\sigma_s^2 - 2\,s_t}{\sqrt{8}\,\sigma_s}\right) + C\,\frac{\exp(s_t(1 - \alpha_{PL}))}{\alpha_{PL} - 1}\right\}, \quad (22)$$

where s_t is the density at which the $n - PDF$ transitions from a lognormal to power-law shape, and N is a normalization factor. We take $s_{thresh} \equiv s_t$.

(c) We adopt s_t as the threshold density for the Burkhart (2018) formalism, which is given in

Burkhart & Mocz (2019) as

$$s_t = (\alpha_{PL} - 1/2)\sigma_s^2. \quad (23)$$

In this formalism, s_t is tied to the slope of the power-law component of the n-PDF, as well as to the width of the lognormal component.

(d) For the LN+PL models, f_{grav} is given by Equation (20) in Burkhart & Mocz (2019; which is referred to as f_{dense} in their work).

3. Fixed density-threshold models:

(a) These models have a lognormal (LN) $n - PDF$ (see Equation (15)).

(b) We again use Equation (13) from Burkhart (2018) to calculate ϵ_{ff}.

(c) We use a fixed density threshold of $n_{SF} = 10^{4.5}$ cm^{-3}.

(d) We perform a numerical integration of the $n - PDF$ above n_{SF} to calculate f_{grav}.

We hereafter refer to these three models as (1) LN PN11, (2) LN+PL B18, and (3) LN Fixed.

3.2. Predictions of Analytical Models

Each of the models above has a unique prescription for f_{grav} depending on n_{SF} and the shape of the $n - PDF$, and this has an impact on their predictions of star formation. The simplest prescription for f_{grav} is that of fixed density-threshold models, which predict that $n_{SF} \approx 10^{4.5}$ cm^{-3}. In this context, the fraction of star-forming gas is any gas above this density. For purely lognormal $n - PDFs$, increases in the width of the $n - PDF$, σ_n, and mean density will both contribute to higher f_{grav} and subsequently higher ϵ_{ff}. This model implies that the SFR is set solely by the mass available above $n_{SF} \approx 10^{4.5}$ cm^{-3}, and that the depletion time of this dense gas mass is constant.

A fixed density threshold also has several other testable predictions:

1. Higher $\mathcal{M}$ increases σ_v and so contributes to higher f_{grav}, shorter total gas depletion times, and ultimately, higher Σ_{SFR}. As a result, for a given $\mathcal{M}$, only the increase in gas mass (Σ_{mol}) is important for increasing Σ_{SFR}.

2. Higher mean densities correlate with higher f_{grav}, shorter total gas depletion times, and ultimately, higher Σ_{SFR}.

The Burkhart (2018) and Padoan & Nordlund (2011) models predict that n_{SF} varies, but these formalisms have different interpretations as to why this variation occurs. Burkhart (2018) argue that variations in ϵ_{ff} may largely be linked to evolutionary changes in the $n - PDF$ shape such that the $n - PDF$ evolves from a lognormal shape to a composite lognormal and power law over time, and the power-law tail develops a shallower slope as more gas becomes gravitationally bound (see Ballesteros-Paredes et al. 2011).

There is a dependence also on turbulence similar to that of the Padoan & Nordlund (2011) model, but Burkhart (2018) argue that this dependence becomes less important as clouds become more evolved (i.e., α_{PL} becomes more shallow). The Burkhart (2018) model does not depend explicitly on α_{vir} either, whereas virialization of the gas is included in the Padoan & Nordlund (2011) definition of n_{SF}.

In the Burkhart (2018) and Padoan & Nordlund (2011) models, higher $\mathcal{M}$ has the effect of increasing n_{SF}. Based on this, the following qualitative predictions can be made about both of these models:

---

[10] This formula is almost identical to the Krumholz & McKee (2005) formalism for ϵ_{ff} when we remove the exponential factor containing s_{thresh}.

[11] This equation is nearly identical to the Krumholz & McKee (2005) formalism, which has a prefactor $\pi/15$ (assuming $\phi_t = 1$).

[12] n_{SF} is referred to as n_{crit} in Padoan & Nordlund (2011) and Burkhart (2018), not to be confused with the critical density for a molecular transition.
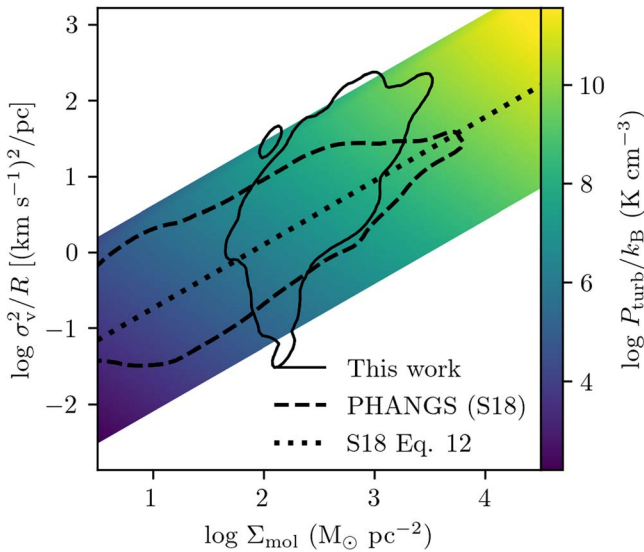
Figure 1. The grid of cloud coefficients, σ_v/R^2, (see Heyer et al. [2009]) and molecular gas surface densities, Σ_{mol}, used as inputs to the lognormal-only analytical models, colored by turbulent pressure, P_{turb}. The x-axis is proportional to the model mean density. The data are shown as the contour density plots, and our sample is contained within the solid black line and the locus of the Sun et al. ([2018]) cloud-scale measurements as the dashed black contour. We use Equation (12) from Sun et al. ([2018]) to define the mean relation between Σ_{mol} and σ_v in our model parameter space (dotted black line).

1. Clouds with higher $\mathcal{M}$ (higher P_{turb}) can have a broader $n - $PDF and higher n_{SF}, lower f_{grav}, lower star formation efficiencies, and ultimately, smaller Σ_{SFR}.
2. Higher temperatures reduce $\mathcal{M}$ and may decrease n_{SF} and potentially increase f_{grav} and enhance star formation efficiencies. This effect will likely be much smaller than changes in P_{turb}, which can span >5 orders of magnitude, compared to T_{kin}, which can only span ∼2 orders of magnitude.

We note that the main difference between the predictions for a fixed n_{SF} and one that varies as $n_{SF} \propto \mathcal{M}^2$ is whether $\mathcal{M}$ directly enhances or suppresses star formation. For the LN+PL B18 models, lower values of α_{PL} (i.e., shallower slopes) will result in more mass in the power-law tail and higher f_{grav}, which will ultimately enhance ϵ_{ff}. We consider these differences when we compare the predictions of these analytical models with our data in the Section 4.

3.3. Connecting Observations to Theory

To compare models with data from our sample, we create a sets of models for each of the three unique prescriptions. We produce LN models over the $\sigma_v^2/R - \Sigma_{mol}$ parameter space that encompasses our data in Figure 1. For comparison, we also show the Sun et al. ([2018]) measurements of cloud-scale observations in nearby galaxies in Figure 1. The mean trend of this parameter space is the empirical trend between velocity dispersion and molecular gas surface density found by Sun et al. ([2018]) for a subset of PHANGS galaxies at cloud scales,

$$\log_{10}\left(\frac{\sigma_v}{\text{km s}^{-1}}\right) = \log_{10}\left(\frac{\Sigma_{mol}}{10^2 \, M_\odot \text{pc}^{-2}}\right) + 0.85. \quad (24)$$

This is shown in Figure 1 as the dotted line. Sun et al. ([2018]) assume a radius of 40 pc for their sources. Because we assume

a fixed LOS depth of 100 pc, we scale the right side of Equation (24) by a factor of $\sqrt{100 \text{ pc}/40 \text{ pc}}$.

The vertical spread in Figure 1 is from variations in σ_v that we consider for the LN models, and it roughly reproduces the spread in $\sigma_v^2/R - \Sigma_{mol}$ seen in the Sun et al. ([2018]) sample as well as in our sample of galaxies. For the LN+PL B18 models, we impose Equation (24) and consider a range of $\alpha_{PL} = 1.0–2.3$, instead of the range in σ_v considered for the LN models.

We note that the observational efficiency is estimated by taking the ratio of the freefall time to the depletion time, $\epsilon_{ff} = t_{ff}/t_{dep}$. As Burkhart & Mocz ([2019]) point out, a more physically meaningful efficiency for observations of individual star-forming clouds may be the local instantaneous efficiency of star formation at time t, $\epsilon_{inst} \approx \epsilon_0(t)f_{grav}(t)$, where $\epsilon_{inst} < \epsilon_{ff}$. This in particular applies to clouds that have evolved sufficiently to have a power-law tail, where f_{grav} is the fraction of mass that is gravitationally bound (and therefore in the power-law tail). ϵ_{ff} itself is an average of the star formation efficiency of a cloud over the freefall time, which is not directly observable. For simplicity, we assume that our observational estimates of ϵ_{ff} are indeed sensitive to the theoretical definition of ϵ_{ff}. We also compare observational trends of ϵ_{ff} with model trends of $f_{grav} \propto \epsilon_{inst}$.

We adopt a constant local efficiency of $\epsilon_0 = 1\%$ for all models. This value of ϵ_0 is consistent with estimates of ϵ_{ff} from observations, and simulations imply low efficiencies, which range from $0.01 - \lesssim 20\%$ (Evans et al. [2009]; Lada et al. [2010]; Ostriker & Shetty [2011]; Krumholz [2014]; Zamora-Avilés & Vázquez-Semadeni [2014]; Lee et al. [2016]; Semenov et al. [2017]; Grudić et al. [2018]). We summarize the observational measurements and the quantities that we estimate from them in the top half of Table 2. In the bottom half of Table 2, we list the equations used to estimate the same quantities using model outputs.

4. Results

In this section, we review general trends between observation-based quantities and the predictions of those from analytical models of star formation. We present a series of plots showing the observational quantities listed in the top half of Table 2 that we use to compare against the model predictions described in the bottom half of Table 2. We focus on variations in star formation timescales (depletion time and freefall time), star formation efficiency, and the dense gas fraction. We do not directly assess variations in emissivity in this paper and defer an analysis of emissivity (and therefore conversion factors) to Bemis ([2020]) and Bemis & Wilson (in prep.), where we present a modeling of the HCN and CO emissivities for our sample of galaxies on a pixel-by-pixel basis.

The results from analytical models are compared to the data in Figures 2–11. We consider fiducial models that correspond to the parameters that best fit the observed Kennicutt–Schmidt relation (KS; see Figure 3). For each model, we calculate the χ^2 of the data relative to this fiducial model, and this value is shown in each panel. We note that the best-fit value for α_{PL} is 1.9 for the LN+PL models. The best-fit relation between $\Sigma_{mol} - \sigma_v$ for the LN-only models is in agreement with the Sun et al. ([2018]) relation (Equation (24)) within the uncertainty.

We show separate plots with the data and their measurement uncertainties alone, followed by plots comparing the data with the models. We refer to Spearman rank coefficients as a

Table 2
Observational Quantities (Top Panel) Compared to Model Inputs and Outputs (Bottom Panel)

	Observational Estimate	Equation	Unit
	$\Sigma_{\rm mol,obs}$	$\alpha_{\rm CO}(I_{\rm CO}/{\rm K~km~s^{-1}})$	$M_\odot~{\rm pc^{-2}}$
	$\Sigma_{\rm mol,dense,obs}$	$3.2~\alpha_{\rm CO}(I_{\rm HCN}/{\rm K~km~s^{-1}})$	$M_\odot~{\rm pc^{-2}}$
(1)	$\Sigma_{\rm SFR,obs}$	$1.14\times10^{-29}(L_{\rm 93~GHz}/{\rm erg~s^{-1}~Hz})$	$M_\odot~{\rm yr^{-1}}$ ${\rm kpc^{-2}}$
(2)	$P_{\rm turb,obs}$	$(3/2)\Sigma_{\rm mol}\sigma_{\rm v}^2/R/k_B$	${\rm K~cm^{-3}}$
(3)	$t_{\rm dep,obs}$	$\Sigma_{\rm mol}/\Sigma_{\rm SFR}$	yr
	$n_{\rm 0,obs}$	$\Sigma_{\rm mol}/R$	${\rm kg~cm^{-3}}$
	$t_{\rm ff,obs}$	$\sqrt{3\pi/32\,G\,n_{\rm 0,obs}}$	yr
(4)	$\epsilon_{\rm ff,obs}$	$t_{\rm ff,obs}/t_{\rm dep,obs}$	...
(5)	$f_{\rm dense}$	$3.2~I_{\rm HCN}/I_{\rm CO}$	...
(6)	$t_{\rm dep,dense,obs}$	$\Sigma_{\rm mol,dense}/\Sigma_{\rm SFR}$	yr
	Model Estimates	Equation	Unit
(1)	$\Sigma_{\rm SFR,model}$	$\epsilon_{\rm ff,model}\times\Sigma_{\rm mol,grid}/t_{\rm ff,grid}$	$M_\odot~{\rm yr^{-1}}$ ${\rm kpc^{-2}}$
(2)	$P_{\rm turb,model}$	$(3/2)n_0\sigma_{\rm v}^2/k_B$	${\rm K~cm^{-3}}$
(3)	$t_{\rm dep,model}$	$1/\epsilon_{\rm ff,model}\times t_{\rm ff,grid}$	yr
(4)	$\epsilon_{\rm ff,model}$	Equations (13) or (27) in Burkhart (2018)	...
(5)	$f_{\rm grav}$	Equations (1), (20) in Burkhart & Mocz (2019)	...
(6)	$t_{\rm dep,grav}$	$f_{\rm grav}/\epsilon_{\rm ff,model}\times t_{\rm ff,grid}$	yr
(6)	$t_{\rm dep,dense,model}$	$f(n>10^{4.5}~{\rm cm^{-3}})/\epsilon_{\rm ff,model}\times t_{\rm ff,grid}$	yr

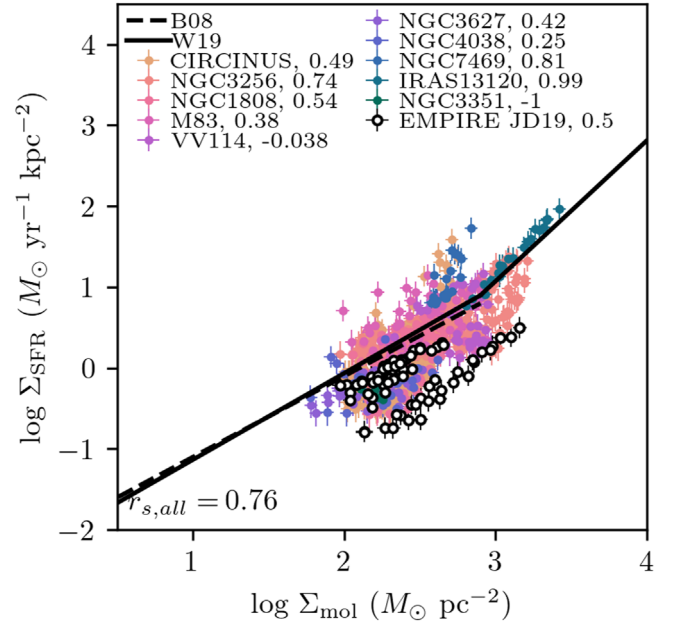**Note.** We number matching observational and model analogs in the leftmost column. We fix $T_{\rm kin}=45$ K, $b=0.4$, and $\beta\to\infty$ in this analysis, and we model over the observed ranges of $\Sigma_{\rm mol}$ and $\sigma_{\rm v}$. Quantities with the subscript "grid" are input from the grid shown in Figure 1.
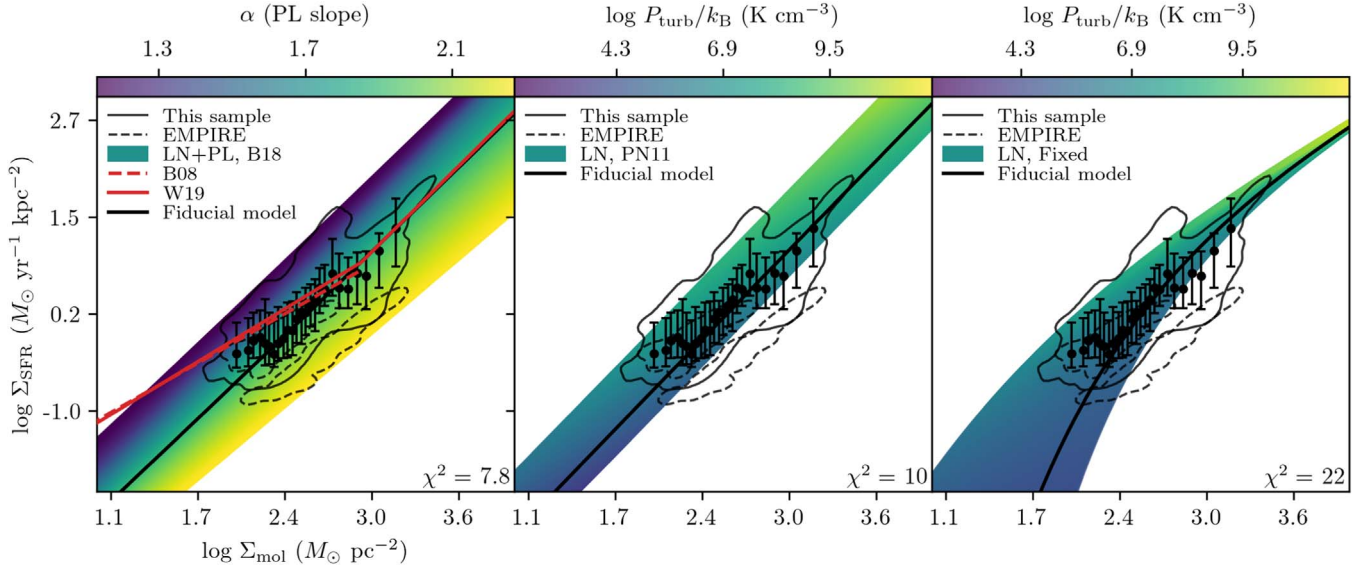

Figure 2. The KS relation for our galaxies and the EMPIRE sample. Data are shown for our sample (colored by galaxy) and the EMPIRE galaxies (white points). We also include fits to this relation from previous studies (e.g., nearby disk galaxies from Bigiel et al. 2008, B08; and (U)LIRGs from Wilson et al. 2019, W19). Spearman rank coefficients are shown for individual galaxies next to their name in the legend, and the coefficient for the combined sample is shown in the lower left corner. On average, the galaxies in the EMPIRE sample have lower $\Sigma_{\rm SFR}$ than the galaxies in our sample, despite similar gas surface densities. Compared to the normal disk galaxies of the EMPIRE sample, the galaxies in our sample are more extreme and include mergers, U/LIRGs, and galaxy centers (see Table 1.)

measure of the strength and direction of correlations between two parameters. For reference, a coefficient of $r_s=0$ indicates that there is no monotonic relation between the two parameters, negative values indicate negative monotonic relations, and positive values indicate positive monotonic relations. In the following discussion, we use the following definitions: $0.1\leqslant|r_s|<0.4$ is considered a weak correlation, $0.4\leqslant|r_s|<0.7$ is considered a moderate correlation, and $|r_s|\geqslant0.7$ is considered a strong correlation.

4.1. The Kennicutt–Schmidt Relation

We begin by presenting the KS relation of our data in Figure 2. In Figure 3 we compare the data to model predictions of $\Sigma_{\rm SFR}$, which are determined using the relevant equation in Table 2 and the parameter spaces discussed in Section 3.3.

1. *LN PN11:* The LN models with the varying Padoan & Nordlund (2011) threshold produce a steeper relation than observed at lower gas surface densities. The (U) LIRGs studied in Wilson et al. (2019) show a double power-law KS relation, with lower $\Sigma_{\rm mol}$ galaxies returning a slope close to unity, similar to the results of Bigiel et al. (2008). The higher-$\Sigma_{\rm mol}$ galaxies instead have a steeper KS slope of 1.74. For the parameter space we consider, the trend of the KS relation predicted by the PN11 models agrees with a slope >1.

2. *LN+PL B18:* Similar to the PN11 models, the LN+PL B18 models produce a steeper relation than observed at

lower gas surface densities and match the steep slope observed by Wilson et al. (2019) for U/LIRGs. We find larger $\alpha_{\rm PL}$ results in lower $\Sigma_{\rm SFR}$ (left panel of Figure 3), in agreement with the predictions from Burkhart (2018). Burkhart (2018) argue that larger $\alpha_{\rm PL}$ results in lower $\epsilon_{\rm ff}$ (and higher $\Sigma_{\rm SFR}$), which is seen for some Milky Way clouds.

3. *LN Fixed:* These fixed-threshold models produce a trend in $\Sigma_{\rm SFR}$ with $\Sigma_{\rm mol}$ that is not seen in the data. Lower $\Sigma_{\rm mol}$ values produce a steeper KS relation, while higher $\Sigma_{\rm mol}$ produce a shallower KS relation; this contradicts observations.

Figure 3 demonstrateszzz that each model is able to reproduce some of the scatter in the KS relations when variations in $\alpha_{\rm PL}$ (LN+PL B18 models) and $\sigma_{\rm v}$ (LN models) for a given gas surface density are considered. No models produce a multislope KS relation consistent with the slopes measured in previous studies (e.g., Wilson et al. 2019). However, we note that changing the slope of the imposed relation between $\sigma_{\rm v}$ and $\Sigma_{\rm mol}$ (Figure 1) has the effect of changing the slope of the KS relation for all of these models. Lower slopes, e.g., $\log\sigma_{\rm v}\propto0.1\log\Sigma_{\rm mol}$, produce a shallower KS relation. We cannot exclude the possibility that other model parameters (i.e., b, β, and $T_{\rm kin}$) may have underlying trends with $\Sigma_{\rm mol}$ or $\sigma_{\rm v}$, which in turn might also produce a varying KS slope. Additionally, ϵ_0 could vary with $\Sigma_{\rm mol}$, for example, if a higher $\Sigma_{\rm SFR}$ results in higher stellar feedback and a lower ϵ_0. Variations in power-law slope may also contribute to changes in the slope of the KS relation. Federrath & Klessen (2013) find that decreases in power-law slope coincide with enhanced star

Figure 3. The KS relation for our galaxies (solid black contours) and the EMPIRE sample (dashed black contours), compared to the model predictions. We also include fits to this relation from previous studies (see the caption of Figure 2). The three models we consider in this analysis are the LN+PL B18 model with varying n_{SF} (left), the LN model with the Padoan & Nordlund (2011) n_{SF} (center), and the LN model with a fixed $n_{SF} = 10^{4.5}$ cm^{-3} (right). The LN+PL B18 models are colored by α_{PL}, and the LN models are colored by P_{turb}. χ^2 relative to the fiducial model is shown in the lower right corner of each plot. The median values of the data are shown with the black data points, and the error bars correspond to the 1σ spread in each bin. Each model is able to reproduce some of the scatter of the KS relation when considering variations in α_{PL} (LN+PL B18 models) and $P_{turb} \propto \sigma_v^2$ (LN models) for a given gas surface density.
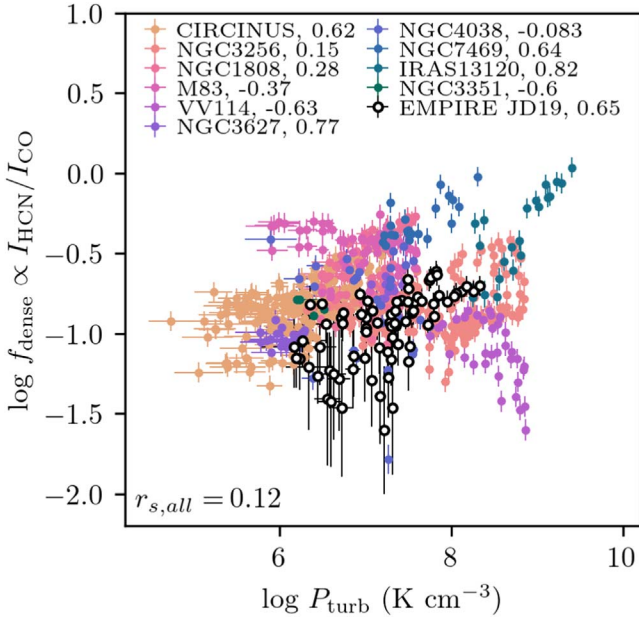
Figure 4. Dense gas fraction as a function of turbulent pressure for our galaxies and the EMPIRE sample, where $f_{dense} = \alpha_{HCN}/\alpha_{CO} I_{HCN}/I_{CO}$. Correlation coefficients are shown, and the data are colored by galaxy, similar to the formatting in Figure 2. The sample as a whole shows a weak positive correlation between f_{dense} traced by I_{HCN}/I_{CO} and P_{turb}. The disk galaxies in the EMPIRE sample show a strong positive correlation.

formation efficiencies and vice versa (Federrath & Klessen 2013; Burkhart & Mocz 2019), and that this is a reflection of the increased fraction of dense gas that coincides with shallow power-law slopes. To match the shallower slope of the KS relation at gas surface densities below $\Sigma_{mol} \approx 10^{2.9} M_{\odot} pc^{-2}$ (e.g., Bigiel et al. 2008; Wilson et al. 2019; Kennicutt & De Los Reyes 2021), the average power-law slope would need to increase (become steeper) toward higher gas surface densities. This would also imply lower ϵ_0 toward higher Σ_{mol}

(Federrath & Klessen 2013; Burkhart & Mocz 2019). Above $\Sigma_{mol} \approx 10^{2.9} M_{\odot}pc^{-2}$, the steeper KS slope found in Wilson et al. (2019) appears consistent with a constant power-law slope.

4.2. Does HCN/CO Trace the Star-forming Gas Fraction?

We compare the observed dense gas fraction ($f_{dense} = \alpha_{HCN}/\alpha_{CO} I_{HCN}/I_{CO}$) with estimates of turbulent pressure, P_{turb}, in Figure 4. Our data show a weak positive trend between f_{dense} and P_{turb} on average, and this relation also holds within most of the individual galaxies in our sample. We plot model predictions of f_{grav} versus P_{turb} in Figure 5 and show the outline of the data relation between f_{dense} and P_{turb} in the background. For comparison, in the bottom rows of Figure 5, we plot the fraction of gas above a fixed density $n = 10^{4.5}$ cm^{-3} for all of the three model n−PDFs prescriptions.

1. *LN PN11:* The LN varying-threshold models also predict a negative trend between f_{grav} and P_{turb}. On average, f_{grav} is lower than f_{dense} predicted by the data. Similar to the LN+PL B18 models, we see a positive trend between $f(n > 10^{4.5}$ cm$^{-3})$ and P_{turb}. However, there is very little spread in the model $f(n > 10^{4.5}$ cm$^{-3})$ versus P_{turb} relation. This indicates that the spread observed in the f_{dense} versus P_{turb} relation in our data is poorly reproduced by variations in σ_v alone.

2. *LN+PL B18:* For constant α_{PL}, these models predict a negative trend between f_{grav} and P_{turb}, and this becomes steeper for larger α_{PL}. The data primarily overlap with f_{grav} for models with shallower values of α_{PL}. In contrast, we see a positive trend between $f(n > 10^{4.5}$ cm$^{-3})$ predicted by the models and P_{turb}. Lower values of α_{PL} produce a flatter relation between $f(n > 10^{4.5}$ cm$^{-3})$ at low P_{turb}. This results in a broader spread in this relation at lower P_{turb}. In general, the spread observed in the f_{dense}
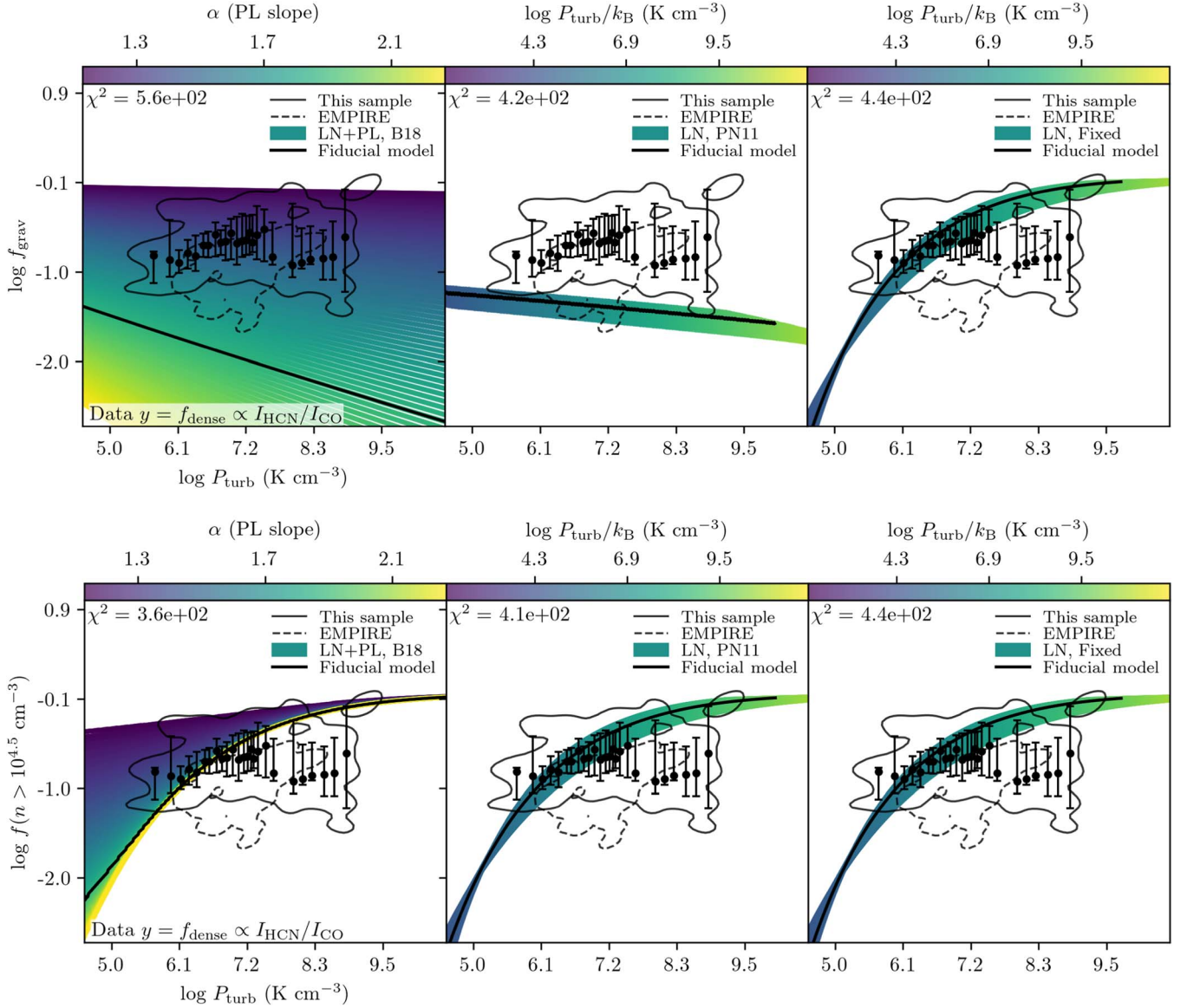
Figure 5. Model f_{grav} (top) and $f(n > 10^{4.5} \text{ cm}^{-3})$ (bottom) as a function of P_{turb}, compared to the data from our sample (solid black contours) and the EMPIRE sample (dashed black contours). Note that $f_{grav} \equiv f_{dense}$ for models with $n_{SF} = 10^{4.5} \text{ cm}^{-3}$. The LN+PL B18 models are colored by α_{PL}, and the LN models are colored by P_{turb}. χ^2 relative to the fiducial model is shown in the upper left corner of each plot. The median values of the data are shown with the black data points, and the error bars correspond to the $1 - \sigma$ spread in each bin. Model f_{grav} decreases with increasing P_{turb} for the models with varying thresholds (i.e., LN+PL B18 and LN P11, left two columns). f_{grav} predicted by the fixed density-threshold models is identical to $f(n > 10^{4.5} \text{ cm}^{-3})$ (right column) and increases with P_{turb}. Model $f(n > 10^{4.5} \text{ cm}^{-3})$ increases with P_{turb} for all models. From this result, the observed positive trend in I_{HCN}/I_{CO} with P_{turb} is more consistent with I_{HCN}/I_{CO} being a better tracer of $f(n > 10^{4.5} \text{ cm}^{-3})$ than f_{grav}.

versus P_{turb} relation in our data is poorly reproduced by variations in α_{PL} alone.

3. *LN Fixed:* f_{grav} predicted by the fixed density-threshold models is identical to $f(n > 10^{4.5} \text{ cm}^{-3})$ because we set the threshold for these models to $n = 10^{4.5} \text{ cm}^{-3}$). As with the other models, we see a positive relation between $f(n > 10^{4.5} \text{ cm}^{-3})$ and P_{turb}. The spread in the data is poorly reproduced by these models.

The predictions of f_{grav} from the varying-threshold models show negative trends with P_{turb} for constant α_{PL} (LN+PL B18 models), in contrast to the positive trends observed with $f(n > 10^{4.5} \text{ cm}^{-3})$ for all models. f_{grav} is equivalent to $f(n > 10^{4.5} \text{ cm}^{-3})$ in the fixed-threshold models. From these results, the weak positive trend of $f_{dense} \propto I_{HCN}/I_{CO}$ with P_{turb} seen in our data is more consistent with the positive trend

between $f(n > 10^{4.5} \text{ cm}^{-3})$ and P_{turb} seen in the models, and it supports the conclusion that I_{HCN}/I_{CO} traces gas above a roughly constant density, but not necessarily the f_{grav} predicted by gravoturbulent models of star formation.

4.2.1. The Star Formation Efficiency per Freefall Time

As a check on the results above, we also consider ϵ_{ff}. In Figure 6 we plot our data as a function of P_{turb} (left panel) and f_{dense} (right panel). In Figure 7 we compare the model predictions of ϵ_{ff} with P_{turb} (top row), $f(n > 10^{4.5} \text{ cm}^{-3})$ (middle row), and f_{grav} (bottom row). ϵ_{ff} shows a weak negative correlation with P_{turb} and a weak positive correlation with f_{dense} (Figure 6) when considering our sample as a whole. These results agree with the qualitative predictions of the varying
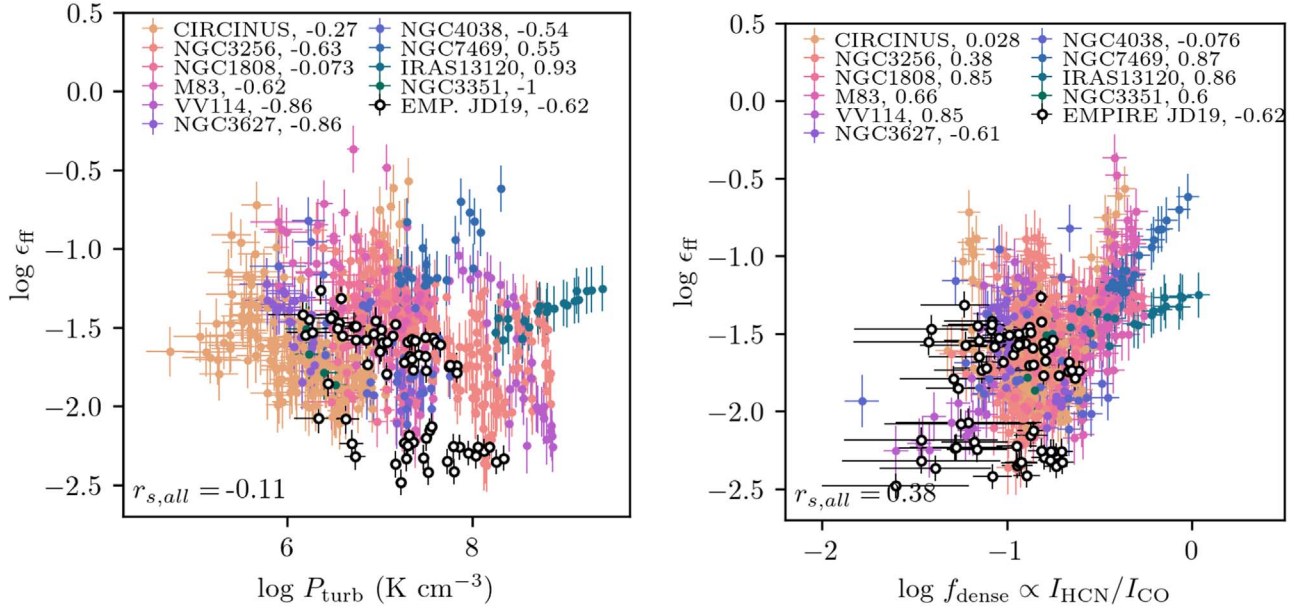
Figure 6. Left: The efficiency per freefall time as a function of $P_{\rm turb}$ for our galaxies and the EMPIRE sample. Correlation coefficients are shown, and the data are colored by galaxy, similar to the formatting in Figure 2. The sample as a whole shows a weak negative correlation between $\epsilon_{\rm ff}$ and $P_{\rm turb}$ The disk galaxies in the EMPIRE sample show a moderate negative correlation. Right: The efficiency per freefall time as a function of $f_{\rm dense} \propto I_{\rm HCN}/I_{\rm CO}$. The sample as a whole shows a moderate positive correlation between $\epsilon_{\rm ff}$ and $f_{\rm dense}$. The EMPIRE sample shows a moderate negative correlation.

density-threshold models (discussed in Section 3), where higher $\mathcal{M} \sim \sigma_{\rm v}$ (and therefore $P_{\rm turb} \sim \sigma_{\rm v}^2$) yields a lower $\epsilon_{\rm ff}$.

1. *LN PN11:* The negative trend between $\epsilon_{\rm ff}$ and $P_{\rm turb}$ seen in the data is not reproduced by the LN PN11 models (middle column, top row of Figure 7). However, the LN PN11 models do reproduce the positive trend between $\epsilon_{\rm ff}$ and $f_{\rm dense}$ seen in the data when we consider $f(n > 10^{4.5}\,{\rm cm}^{-3})$ (middle row of Figure 7). There is some overlap between $\epsilon_{\rm ff}$ and model $f_{\rm grav}$ (bottom row of Figure 7), but this trend does not track the positive relation between $\epsilon_{\rm ff}$ and $f_{\rm dense}$ seen in the data.

2. *LN+PL B18:* Similar to the LN PN11 models, the negative trend between $\epsilon_{\rm ff}$ and $P_{\rm turb}$ seen in the data is not reproduced by any single value of $\alpha_{\rm PL}$ for these models (left column, top row of Figure 7). Rather, the data overlap with these models for a range of $\alpha_{\rm PL}$, with higher values of $\epsilon_{\rm ff}$ corresponding to lower values of $\alpha_{\rm PL}$ and lower $P_{\rm turb}$.

   Moreover, similar to the LN PN11 models, the LN +PL B18 models do reproduce the positive trend between $\epsilon_{\rm ff}$ and $f_{\rm dense}$ seen in the data when we consider $f(n > 10^{4.5}\,{\rm cm}^{-3})$ (middle row of Figure 7). In this case, the vertical spread in the data corresponds to variations in $\alpha_{\rm PL}$. Models with lower $\alpha_{\rm PL}$ also show an upturn in $\epsilon_{\rm ff}$ at higher $f(n > 10^{4.5}\,{\rm cm}^{-3})$ consistent with the trend seen in the data.

   At first look, the positive trend between $\epsilon_{\rm ff}$ and $f_{\rm dense}$ seen in the data also appears consistent with the trend between $\epsilon_{\rm ff}$ and model $f_{\rm grav}$ (bottom row of Figure 7). However, this requires that $f_{\rm dense} \propto f_{\rm grav}$, for which we find evidence to the contrary in the previous section.

3. *LN Fixed:* The fixed-threshold models predict an increase in $\epsilon_{\rm ff}$ with $P_{\rm turb}$ up to $P_{\rm turb} \approx 10^7\,{\rm K}\,{\rm cm}^{-3}$, after which this relation flattens and $\epsilon_{\rm ff}$ slightly turns over. This is not seen in our data. These models predict a positive relation between $\epsilon_{\rm ff}$ and $f_{\rm grav}$ up to $\log f_{\rm grav} \approx -0.5$, above which

$\epsilon_{\rm ff}$ turns over. There is no evidence for this turnover in our data.

The varying-threshold models are able to reproduce the positive trend seen between $\epsilon_{\rm ff}$ and $f_{\rm dense}$ when considering $f(n > 10^{4.5}\,{\rm cm}^{-3})$. Some of the scatter is also reproduced by these models when considering a range in $\alpha_{\rm PL}$ or a range in $\sigma_{\rm v}$ (see Figure 7).

*4.2.2. Total Gas Depletion Times*

Now we consider whether estimates of the total gas depletion times may give insight into the discrepancy between $f_{\rm grav}$ and observational estimates of $f_{\rm dense}$. We plot $t_{\rm dep}$ as a function of $P_{\rm turb}$ and $f_{\rm dense}$ for our sample of galaxies in Figure 8. We find moderate negative correlations between $t_{\rm dep}$ and the dense gas fraction traced by $I_{\rm HCN}/I_{\rm CO}$. $t_{\rm dep}$ estimated from the data appears relatively constant with $P_{\rm turb}$, but the Spearman rank coefficient of the combined data indicates a moderate negative correlation (see Figure 8).

1. *LN PN11:* These models are able to reproduce the average trends seen in our data (i.e., negative trend between $t_{\rm dep}$ and $P_{\rm turb}$ and negative trend between $t_{\rm dep}$ and $f(n > 10^{4.5}\,{\rm cm}^{-3})$). Variations in $P_{\rm turb}$ alone do not reproduce the spread seen in our data. $t_{\rm dep}$ versus $f_{\rm grav}$ does not track the relation between $t_{\rm dep}$ and $f_{\rm dense}$ seen in the data.

2. *LN+PL B18:* We find good agreement between these models and the data when comparing $t_{\rm dep}$, $P_{\rm turb}$, and $f(n > 10^{4.5}\,{\rm cm}^{-3})$ (Figure 9). Although the data overlap with $t_{\rm dep}$ versus $f_{\rm grav}$, the models show a much larger spread than that observed in the data.

3. *LN Fixed:* These models predict that $t_{\rm dep}$ decreases until $P_{\rm turb} \sim 10^7\,{\rm K}\,{\rm cm}^{-3}$ until it reaches a roughly constant value. This behavior is not seen in our data. $t_{\rm dep}$ monotonically decreases with $f(n > 10^{4.5}\,{\rm cm}^{-3})$ and $f_{\rm grav}$ for these models.
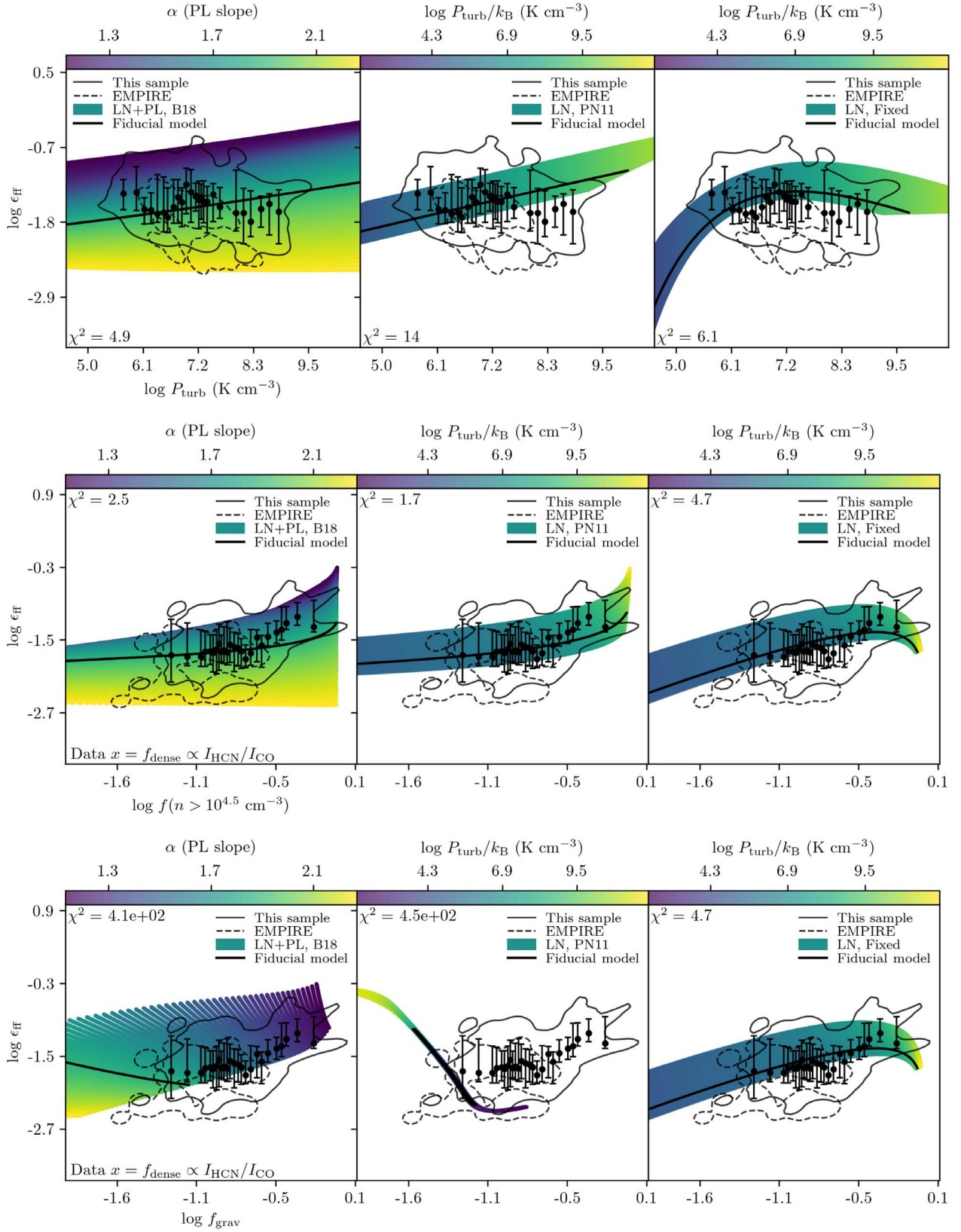
Figure 7. Model ϵ_{ff} as a function of P_{turb} (top), $f(n > 10^{4.5}\ \mathrm{cm}^{-3})$ (middle), and f_{grav} (bottom) compared to data from our sample (solid black contours) and the EMPIRE sample (dashed black contours). See Table 2 for information on how these values are calculated. The LN+PL B18 models are colored by α_{PL}, and the LN models are colored by P_{turb}. χ^2 relative to the fiducial model is shown in the bottom left corner of the plots in the top row and in the upper left corner of the plots in the bottom two rows. The median values of the data are shown with the black data points, and the error bars correspond to the 1σ spread in each bin. The bottom two rows show the importance of distinguishing f_{grav} from $f(n > 10^{4.5}\ \mathrm{cm}^{-3})$ when using $I_{\mathrm{HCN}}/I_{\mathrm{CO}}$ as a tracer of the dense star-forming gas. All models considered agree better with observations when using $f(n > 10^{4.5}\ \mathrm{cm}^{-3})$ as a proxy for the dense gas fraction traced by $I_{\mathrm{HCN}}/I_{\mathrm{CO}}$. See the text for a full analysis of the plots.
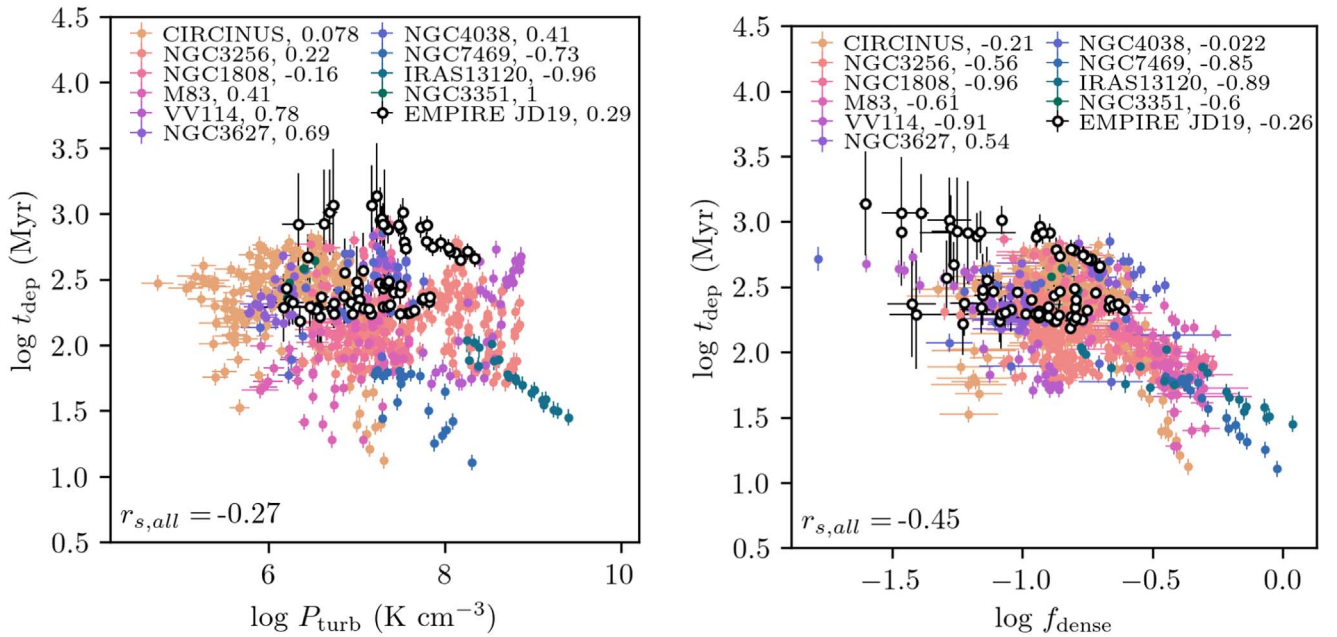
Figure 8. Left: Depletion time of the total molecular gas content as a function of P_{turb} for our galaxies and the EMPIRE sample. Correlation coefficients are shown, and the data is colored by galaxy, similar to the formatting in Figure 2. The sample as a whole shows a weak negative correlation between t_{dep} and P_{turb}. The disk galaxies in the EMPIRE sample show a weak positive correlation. Right: Depletion time of the total molecular gas content as a function of f_{dense} (right). The sample as a whole shows a moderate negative correlation between t_{dep} and P_{turb}. The disk galaxies in the EMPIRE sample show a weak negative correlation. Data are formatted as in Figure 2.

The varying-threshold models best reproduce the observed trend between t_{dep} and P_{turb}. The varying-threshold models also perform better than the fixed-threshold models at reproducing the observed trend between t_{dep} and f_{dense}. Yet again, the trends in the data are best reproduced by the models when considering $f(n > 10^{4.5}\ \mathrm{cm}^{-3})$ rather than f_{grav}.

4.2.3. Dense Gas Depletion Times

We plot the depletion time of the dense gas as traced by HCN, $t_{\mathrm{dep,dense}}$, as a function of P_{turb} (left) and dense gas fraction (right) in Figure 10. We see a moderate positive correlation between $t_{\mathrm{dep,dense}}$ and f_{dense} in ∼3 of our sources and the EMPIRE galaxies. The Spearman rank coefficient shows a weak positive correlation for the combined data set. At first, this appears to contradict the expectation of star formation models, but all models except for those with a fixed threshold are able to roughly reproduce this increase in $t_{\mathrm{dep,dense}}$ with gas fraction (see Figure 11).

1. *LN PN11:* These models predict a turnover in $t_{\mathrm{dep}}(n > 10^{4.5}\ \mathrm{cm}^{-3})$ with P_{turb} and in $t_{\mathrm{dep}}(n > 10^{4.5}\ \mathrm{cm}^{-3})$ with $f(n > 10^{4.5}\ \mathrm{cm}^{-3})$ (see the middle column, top and middle rows in Figure 11). This qualitatively agrees with the average trends seen in our data. We find that $t_{\mathrm{dep,grav}}$ versus f_{grav} does not track the relation between t_{dep} and f_{dense} seen in the data. Variations in P_{turb} alone do not reproduce the spread seen in our data.

2. *LN+PL B18:* For $\alpha_{\mathrm{PL}} > 1.7$, these models predict a turnover in $t_{\mathrm{dep}}(n > 10^{4.5}\ \mathrm{cm}^{-3})$ around $P_{\mathrm{turb}} \sim 10^7$ K cm^{-3} and for $\log f(n > 10^{4.5}\ \mathrm{cm}^{-3}) \sim -0.5$. For $\alpha_{\mathrm{PL}} \leqslant 1.7$, $t_{\mathrm{dep}}(n > 10^{4.5}\ \mathrm{cm}^{-3})$ consistently decreases with P_{turb} and $f(n > 10^{4.5}\ \mathrm{cm}^{-3})$. The observed trends in the data are in qualitative agreement with the trends seen for $\alpha_{\mathrm{PL}} > 1.7$. We include $t_{\mathrm{dep}, grav}$ versus f_{grav} for

completeness, but again find that the models show a much larger spread than is observed in the data.

3. *LN Fixed:* As predicted in Section 3.2, these models return a fixed $t_{\mathrm{dep}}(n > 10^{4.5}\ \mathrm{cm}^{-3})$ regardless of the variations in P_{turb} or $f(n > 10^{4.5}\ \mathrm{cm}^{-3})$.

The LN+PL B18 models are able to qualitatively reproduce the trends observed in $t_{\mathrm{dep,dense}}$, P_{turb}, and f_{dense} for $\alpha_{\mathrm{PL}} > 1.7$. The LN PN11 models are also able to reproduce the average trends, but variations in P_{turb} do not reproduce the observed scatter. These results again refute the interpretation of the $I_{\mathrm{HCN}}/I_{\mathrm{CO}}$ ratio as a a tracer of f_{grav}. The observed trends are best reproduced by the varying-threshold models when considering $f(n > 10^{4.5})\ \mathrm{cm}^{-3}$, but not with f_{grav}, and our results therefore refute this interpretation.

5. Discussion

In this work, we explore how well the HCN-to-CO ratio traces the star-forming fraction of gas in molecular clouds across the more extreme environments of U/LIRGs, mergers, and galaxy centers using gravoturbulent models of star formation (Krumholz & McKee 2005; Hennebelle & Chabrier 2011; Padoan & Nordlund 2011; Federrath & Klessen 2012; Burkhart 2018; Burkhart & Mocz 2019). Previous studies find that HCN may be tracing gas above a fairly constant density and that the mass traced by HCN appears to scale linearly with the SFR, indicating a constant average depletion time of the dense gas that spans clouds (see Wu et al. 2005) to entire galaxies, including disk galaxies and U/LIRGs (see Gao & Solomon 2004a, 2004b). This result is consistent with the predictions of the LN-only models with a fixed threshold that we consider in our analysis (see the right columns of Figures 3, 5, 7, 9, and 11). These models are able to qualitatively reproduce some of the average trends involving the dense molecular gas traced by HCN, such as the decrease in t_{dep} with
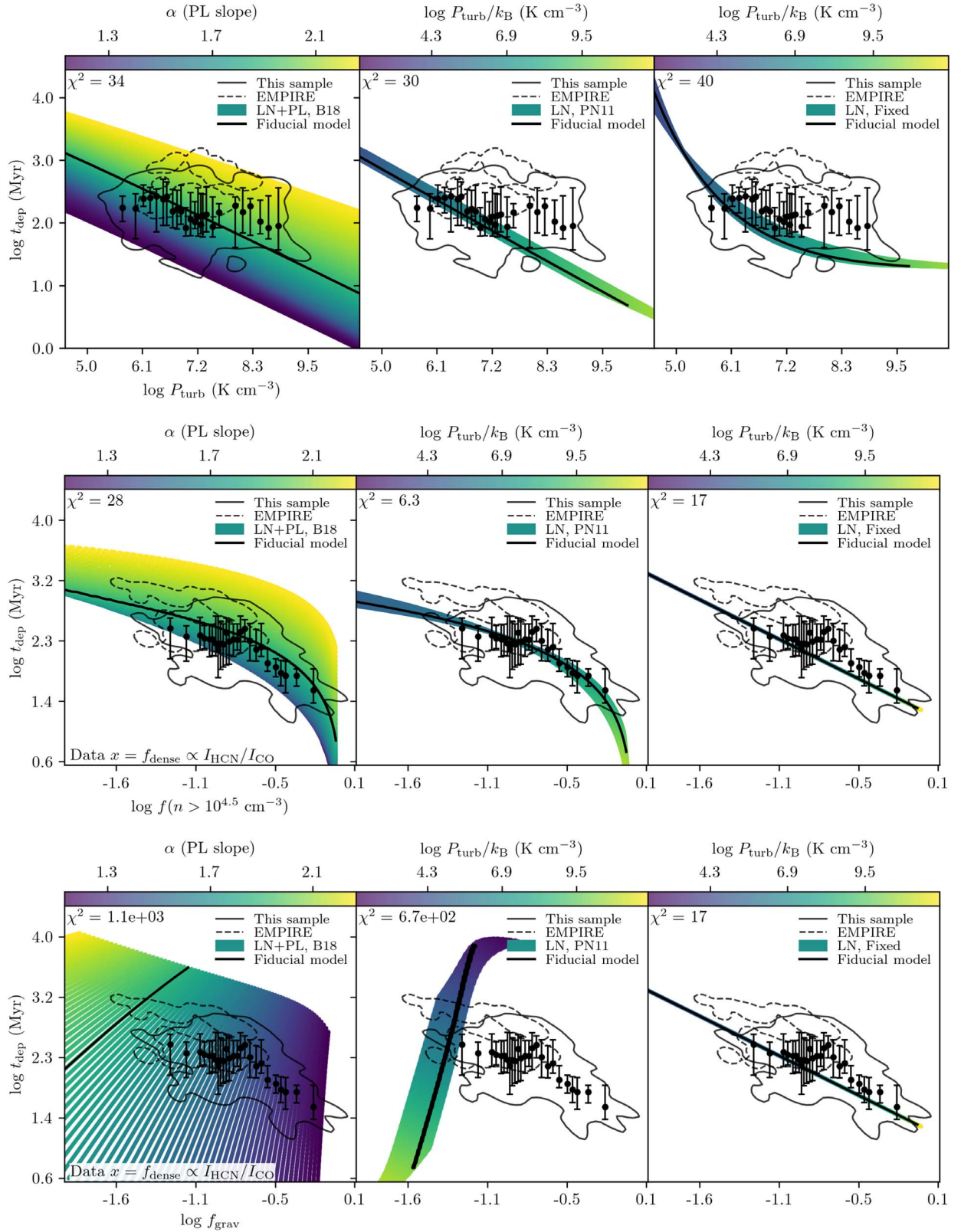
Figure 9. Model t_{dep} as a function of P_{turb} (top), $f(n > 10^{4.5}$ cm$^{-3})$ (middle), and f_{grav} (bottom) compared to the data from our sample (solid black contours) and the EMPIRE sample (dashed black contours). See Table 2 for information on how these values are calculated. The LN+PL B18 models are colored by α_{PL}, and the LN models are colored by P_{turb}. χ^2 relative to the fiducial model is shown in the upper left corner of each plot. The median values of the data are shown with the black data points, and the error bars correspond to the 1σ spread in each bin. Similar to Figure 7, the bottom two rows show the importance of distinguishing f_{grav} from $f(n > 10^{4.5}$ cm$^{-3})$ when using I_{HCN}/I_{CO} as a tracer of the dense star-forming gas. All models considered agree better with observations when using $f(n > 10^{4.5}$ cm$^{-3})$ as a proxy for the dense gas fraction traced by I_{HCN}/I_{CO}. See the text for a full analysis of the plots.
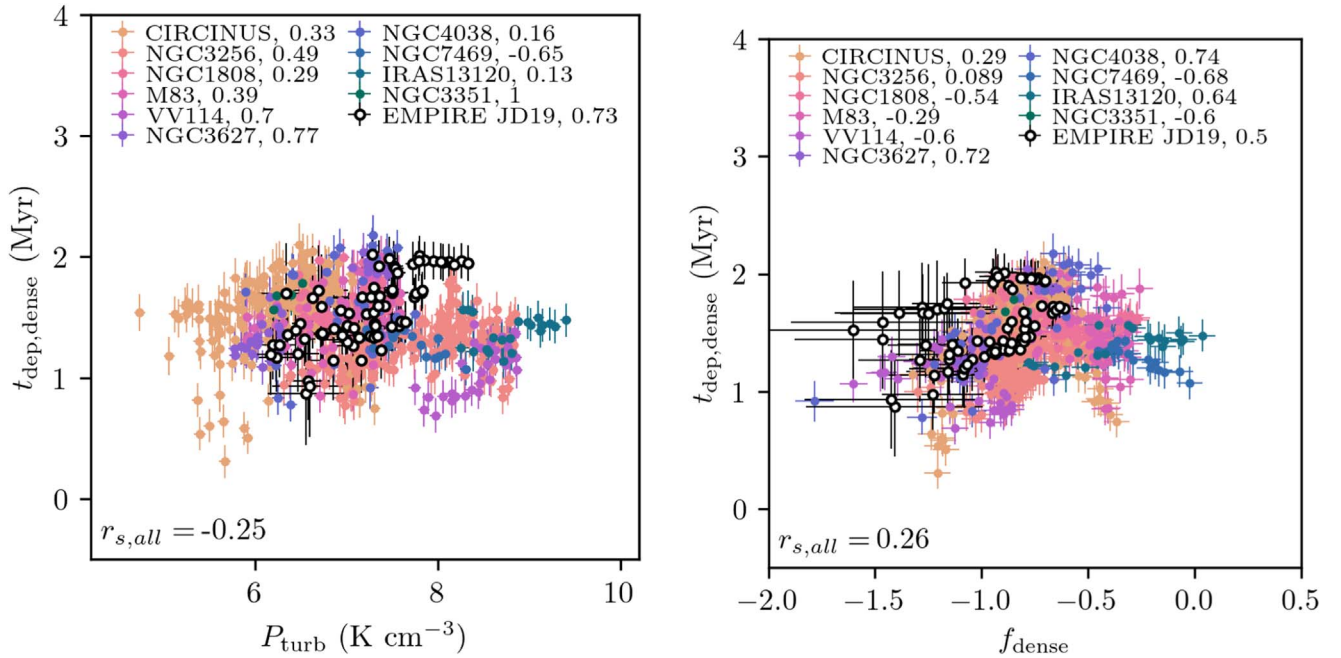
Figure 10. Left: Depletion time of the dense molecular gas content as a function of $P_{\rm turb}$ for our galaxies and the EMPIRE sample. Correlation coefficients are shown, and the data are colored by galaxy, similar to the formatting in Figure 2. The sample as a whole shows a weak negative correlation between $t_{\rm dep,dense}$ and $P_{\rm turb}$. The disk galaxies in the EMPIRE sample show a strong positive correlation. Right: Depletion time of the dense molecular gas content as a function of $f_{\rm dense}$ (right). The sample as a whole shows a weak positive correlation between $t_{\rm dep}$ and $P_{\rm turb}$. The disk galaxies in the EMPIRE sample show a moderate positive correlation. Data are formatted as in Figure 2.

increasing $f_{\rm dense} \propto I_{\rm HCN}/I_{\rm CO}$ (Figure 9). However, these models fail to capture the spread observed in many of the trends of our data and also the observed trends with $P_{\rm turb}$.

The behavior of star formation laws observed in disk galaxies may give some insight into the discrepancy between the fixed-threshold models and observations. There is evidence of nonlinear scalings between dense gas mass and the SFR within disk galaxies that appears to be correlated with galactic radius in disk galaxies (e.g., Chen et al. 2015; Usero et al. 2015; Gallagher et al. 2018). Relative to their disks, the centers of late-type galaxies show longer dense gas depletion times despite larger dense gas fractions traced by $I_{\rm HCN}/I_{\rm CO}$ (e.g., Chen et al. 2015; Usero et al. 2015; Gallagher et al. 2018). Similarly, the nuclei of the merging Antennae galaxies also display longer dense gas depletion times despite higher dense gas fractions compared to the overlap region of this merging system (Bigiel et al. 2015; Bemis & Wilson 2019). Ambient pressure of the ISM is higher in the centers of disk galaxies compared to larger radii, which is apparent from observational estimates of $P_{\rm turb}$ from CO across the disks of nearby disk galaxies (see Gallagher et al. 2018). If higher $P_{\rm turb}$ is indicative of stronger turbulent support, then gravoturbulent models of star formation with varying star formation thresholds may offer an explanation for these observed trends (i.e., Krumholz & McKee 2005; Padoan & Nordlund 2011; Burkhart 2018).

The varying-threshold models considered in this paper (i.e., Padoan & Nordlund 2011; Burkhart 2018) predict that the gas density required for the onset of collapse (and therefore star formation) increases in the presence of supportive processes such as solenoidal turbulence. This is apparent in Figure 5 (left two columns, top row) where the LN+PL B18 and LN P11 models show a decrease in $f_{\rm grav}$ with increasing $P_{\rm turb}$. Turbulence can also increase the mean gas density of the molecular cloud as a whole by widening the $n-$PDF. This is

also apparent in Figure 5 (left two columns, bottom row) where the LN+PL B18 and LN P11 models show an increase in $f(n > 10^{4.5}\,{\rm cm}^{-3})$ with increasing $P_{\rm turb}$. The difference in behavior between $f_{\rm grav}$ and $f(n > 10^{4.5}\,{\rm cm}^{-3})$ with $P_{\rm turb}$ reflects an important prediction of these varying-threshold models: the supportive effect of turbulence can have a more significant impact on star formation than the increase in dense gas mass due to the widening of the $n-$PDF.

A wider $n-$PDF would naturally result in enhanced $I_{\rm HCN}/I_{\rm CO}$ if this ratio were tracing gas above a roughly constant density (see Leroy et al. 2017a; Bemis 2020). At the same time, the SFR itself can appear suppressed relative to the total dense gas mass because the onset of star formation occurs at a higher density than the mean density of the gas traced by $I_{\rm HCN}/I_{\rm CO}$. The results of our work support this picture. In particular, the LN+PL B18 and LN P11 models are able to qualitatively reproduce the average trends observed in our data when considering $f(n > 10^{4.5}\,{\rm cm}^{-3})$ as a proxy for the dense gas fraction traced by $I_{\rm HCN}/I_{\rm CO}$ (see Figures 5, 7, 9, and 11).

One apparent discrepancy between the data and the varying-threshold models is the behavior of $\epsilon_{\rm ff}$ with $P_{\rm turb}$ (see the top row in Figure 7). Our sample shows a weak negative trend between $\epsilon_{\rm ff}$ and $P_{\rm turb}$ and the EMPIRE sample has a moderate negative trend. In contrast, the varying-threshold models predict an increase in $\epsilon_{\rm ff}$ with $P_{\rm turb}$ (see Figure 7). The fixed-threshold LN model predicts that $\epsilon_{\rm ff}$ initially increases with $P_{\rm turb}$ and then decreases toward higher pressures. The discrepancy between the models and data is likely due in part to inaccurate estimates of $t_{\rm ff}$ from our data. When estimating the mean density of the molecular gas traced by CO, we assume a fixed LOS depth of 100 pc for all measurements, including those from the galaxies in the EMPIRE sample. We can also see from Figure 9 that the models predict a steeper decline in $t_{\rm dep}$ with $P_{\rm turb}$ than what is observed in the data.
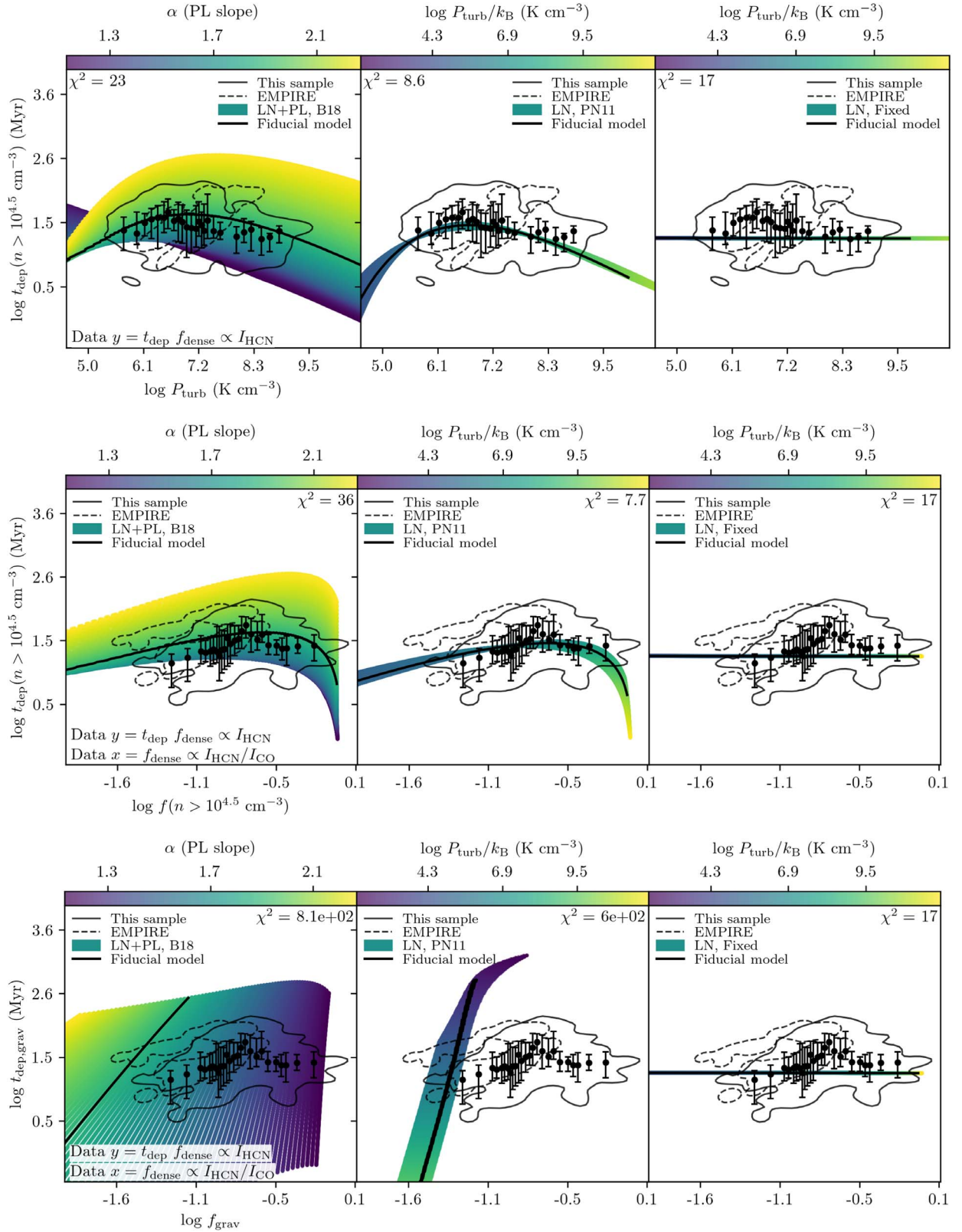
Figure 11. Top two rows: Depletion time of the molecular gas above $n = 10^{4.5}$ cm^{-3} as a function of $P_{\rm turb}$ (top) and $f(n > 10^{4.5}$ cm^{-3}) (middle). Bottom row: Depletion time of the gravitationally bound molecular gas as a function of $f_{\rm grav}$. These trends are compared against our data (solid black contours) and the EMPIRE sample (dashed black contours). See Table 2 for information on how these values are calculated. The LN+PL B18 models are colored by $\alpha_{\rm PL}$, and the LN models are colored by $P_{\rm turb}$. χ^2 relative to the fiducial model is shown in the upper left corner of the plots in the top row and in the upper right corner of the plots in the bottom two rows. The median values of the data are shown with the black data points, and the error bars correspond to the 1σ spread in each bin. All models considered agree better with observations when using $f(n > 10^{4.5}$ cm^{-3}) as a proxy for the dense gas fraction traced by $I_{\rm HCN}/I_{\rm CO}$. See the text for a full analysis of the plots.

These two things combined likely contribute to the discrepancy between the data and the models when considering ϵ_{ff} as a function of P_{turb}. Due to the weakness of the observed trend in our data and the uncertainty in t_{ff}, it is difficult to determine whether ϵ_{ff} truly increases or decreases with P_{turb}. The apparent agreement between ϵ_{ff} and $f(n > 10^{4.5}\,\text{cm}^{-3})$ predicted by the varying-threshold models and our data may then be a reflection of the stronger connection between star formation and denser gas that is better traced by HCN relative to the bulk molecular gas traced by CO (see Gao & Solomon 2004a, 2004b).

We also find that the scatter of the data is only poorly reproduced by variations in P_{turb} when considering the LN-only models (e.g., Figures 5, 7, 9, and 11). One parameter that we did not vary in this analysis is α_{vir}. We consider here how this would impact our results. For the Padoan & Nordlund (2011) models, higher α_{vir} increases n_{SF} such that more unbound clouds will have lower ϵ_{ff}. Variations in α_{vir} would introduce some scatter into the results, primarily in the relations that depend on ϵ_{ff} and t_{dep}. However, variations in $\mathcal{M}$ have an impact on both the width of the $n-$PDF (Equation (17)) and the shift in n_{SF} (Equation (19)) for the LN PN11 models, while changes in α_{vir} primarily have an impact on n_{SF}. Changes in the dense gas fraction indicated by $f(n > 10^{4.5}\,\text{cm}^{-3})$ are not analytically dependent on α_{vir} and therefore would need an additional explanation.

The LN+PL B18 models offer an alternative explanation for the scatter of the data: variations in power-law slope (α_{PL}). Simulations show that a power-law tail develops as a consequence of cloud evolution as gas becomes self-gravitating, and the slope of the power-law tail becomes more shallow as the fraction of bound gas (i.e., f_{grav}) increases (see Ballesteros-Paredes et al. 2011; Collins et al. 2012; Schneider et al. 2015; Burkhart et al. 2017; Padoan et al. 2017). This is supported by observations of some Milky Way clouds, which show a power-law tail at high densities (e.g., Kainulainen et al. 2009; Schneider et al. 2013; Lombardi et al. 2015; Schneider et al. 2015, 2016; Alves et al. 2017). Additionally, there is observational evidence for a connection between power-law slope and ϵ_{ff} that matches the predictions of the LN+PL B18 models (Federrath & Klessen 2013; Burkhart & Mocz 2019).

The scatter in our data is well reproduced for $\alpha_{PL} = 1$–2.3 (see the left column of Figures 3, 5, 7, 9, and 11). These models are also able to reproduce the average trends of our data. Out of the three models we consider, the LN+PL B18 models perform best at reproducing the observational trends and scatter of our data and the EMPIRE sample. In the context of the LN+PL B18 models, the scatter in our data is therefore driven in part due to cloud evolution (Ballesteros-Paredes et al. 2011), such that the $n-$PDF of clouds evolves from a lognormal shape to a composite lognormal and power law over time as more gas becomes gravitationally bound. The underlying trends are still driven largely by variations in turbulence, which we impose in our model parameter space by using the observational relation between gas surface density and velocity dispersion found by Sun et al. (2018; see Equation (24)).

6. Conclusions

We find the following conclusions from our comparison between observation and the predictions of analytical models of star formation:

1. KS relation: For the model parameter space considered, none of the models reproduce the multislope KS relation as found in Wilson et al. (2019). Variations in the slope of the $\Sigma_{mol} - \sigma_v$ relation can produce variations in the KS slope, such that a shallower (steeper) $\Sigma_{mol} - \sigma_v$ relation would produce a shallower (steeper) KS relation. Furthermore, systematic changes in ϵ_0 or power-law slope with Σ_{mol} could also affect the KS slope. An increasing (decreasing) power-law slope with Σ_{mol} would produce a shallower (steeper) KS relation. Similarly, a decreasing (increasing) ϵ_0 with Σ_{mol} produces a shallower (steeper) KS slope.

2. f_{dense} and f_{grav}: For the PN11 and B18 models, f_{grav} decreases with P_{turb} and increases for the fixed-threshold models. $f(n > 10^{4.5}\,\text{cm}^{-3})$ increases with P_{turb} for all models. The behavior of $f(n > 10^{4.5}\,\text{cm}^{-3})$ with P_{turb} is in qualitative agreement with our data, which show an increase in $f_{dense} = (\alpha_{HCN}/\alpha_{CO})I_{HCN}/I_{CO}$ with observational estimates of P_{turb}. We therefore conclude that the I_{HCN}/I_{CO} ratio likely does not track f_{grav} as predicted by the varying-threshold models, but rather the fraction of gas above some fixed density, such as $f(n > 10^{4.5}\,\text{cm}^{-3})$.

3. ϵ_{ff}: For the PN11 and B18 models, ϵ_{ff} increases with P_{turb} on average. For the fixed-threshold models, ϵ_{ff} increases with P_{turb} until $P_{turb}/k_B \approx 10^{7.5}\,\text{K cm}^{-3}$ where it turns over. All models predict an increase in ϵ_{ff} with $f(n > 10^{4.5}\,\text{cm}^{-3})$, on average, with only the fixed-threshold models showing a turnover in this relation at high fractions. ϵ_{ff} decreases with f_{grav} for the the PN11 models and the B18 models for fixed α_{PL}. For the fixed-threshold models, ϵ_{ff} increases with f_{grav} until it turns over at high fractions. Under the assumption of a fixed LOS depth, our data show a weak decrease in ϵ_{ff} with P_{turb} and increase with f_{dense}. This is in qualitative agreement with the PN11 and B18 models, assuming I_{HCN}/I_{CO} is tracking $f(n > 10^{4.5}\,\text{cm}^{-3})$, but not f_{grav}.

4. Total gas depletion time: All models predict a decrease in t_{dep} with both P_{turb} and $f(n > 10^{4.5}\,\text{cm}^{-3})$. The fixed-threshold models predict a flattening of t_{dep} with higher P_{turb}, but a constant decrease with $f(n > 10^{4.5}\,\text{cm}^{-3})$. In contrast, the PN11 models and the B18 models show a constant decrease in t_{dep} with P_{turb}, but a steepening decline in t_{dep} with higher $f(n > 10^{4.5}\,\text{cm}^{-3})$. t_{dep} increases with f_{grav} for the PN11 models and the B18 models for fixed α_{PL}. The trends in data are in better qualitative agreement with the PN11 and B18 models, again assuming I_{HCN}/I_{CO} is tracking $f(n > 10^{4.5}\,\text{cm}^{-3})$, but not f_{grav}.

5. Dense gas depletion time: The PN11 and B18 models (for $\alpha_{PL} > 1.7$) predict a turnover in the depletion time of dense gas, $t_{dep}(n > 10^{4.5}\,\text{cm}^{-3})$, with P_{turb} and $f(n > 10^{4.5}\,\text{cm}^{-3})$, while the fixed-threshold models predict a constant dense gas depletion time (Gao & Solomon 2004a, 2004b). We note that $\alpha_{PL} < 1.7$ produces a nearly constant decrease in $t_{dep}(n > 10^{4.5}\,\text{cm}^{-3})$ with P_{turb} and $f(n > 10^{4.5}\,\text{cm}^{-3})$. $t_{dep,grav}$ increases with f_{grav} for the PN11 models and the B18 models for fixed α_{PL}. The trends in data are in better qualitative agreement with the PN11 and B18 models, again assuming I_{HCN}/I_{CO} is tracking $f(n > 10^{4.5}\,\text{cm}^{-3})$, but not f_{grav}.

6. Variations in PL slope (α_{PL}) (lognormal+power-law B18 models) are able to explain the scatter in the data. The scatter in our data is only poorly reproduced by variations in P_{turb} (or $\mathcal{M}$) alone.

7. The varying-threshold models (lognormal+power-law B18 and lognormal-only PN11) are able to better reproduce the average trends of our data and the EMPIRE sample compared to the fixed-threshold lognormal-only models.

8. The average trends in the data with P_{turb} and f_{dense} are likely set by variations in turbulence determined by local environment within each galaxy.

In summary, the HCN/CO ratio likely is a reliable tracer of gas above a constant density, such as $n_{\mathrm{SF}} \approx 10^{4.5}$ cm^{-3}, but not necessarily f_{grav}. If varying thresholds for star-forming gas exist in nature, then the HCN/CO ratio is a poor tracer of f_{grav}.

Appendix
Moment Maps and Uncertainties

We use the following expressions to calculate moments and their corresponding uncertainties:

$$\text{MOMENT0:} \quad I = \Sigma_i T_i \Delta v \tag{A1}$$

$$\delta I = \delta \bar{T} \Delta v \sqrt{N_{\mathrm{chan}}} \tag{A2}$$

$$\text{MOMENT1:} \quad \bar{v} = \frac{\Sigma_i T_i v_i}{\Sigma_i T_i} \tag{A3}$$

$$\delta \bar{v} = \frac{N_{\mathrm{chan}} \Delta v}{2\sqrt{3}} \frac{\delta I}{I} \tag{A4}$$

$$\text{MOMENT2:} \quad \sigma_v = \sqrt{\frac{\Sigma_i T_i (v_i - \bar{v})^2}{\Sigma_i T_i}} \tag{A5}$$

$$\delta \sigma_v = \frac{\delta_I}{I} \frac{(N_{\mathrm{chan}} \Delta v)^2}{8\sqrt{5}} \frac{1}{\sigma_v}. \tag{A6}$$

A full derivation of the uncertainties on Equations (A4) and (A6) is given in Wilson et al. (2023).

ORCID iDs

Ashley R. Bemis ⊙ https://orcid.org/0000-0003-0618-8473
Christine D. Wilson ⊙ https://orcid.org/0000-0001-5817-0991

References

Alves, J., Lombardi, M., & Lada, C. J. 2017, A&A, 606, L2
André, P., Revéret, V., Könyves, V., et al. 2016, A&A, 592, A54
Aniano, G., Draine, B. T., Gordon, K. D., & Sandstrom, K. 2011, PASP, 123, 1218
Astropy Collaboration, Price-Whelan, A. M., Sipőcz, B. M., et al. 2018, AJ, 156, 123
Astropy Collaboration, Price-Whelan, A. M., Lim, P. L., et al. 2022, ApJ, 935, 167
Astropy Collaboration, Robitaille, T. P., Tollerud, E. J., et al. 2013, A&A, 558, A33
Ballesteros-Paredes, J., Vázquez-Semadeni, E., Gazol, A., et al. 2011, MNRAS, 416, 1436
Bemis, A., & Wilson, C. D. 2019, AJ, 157, 131
Bemis, A. R. 2020, PhD thesis, McMaster Univ., http://hdl.handle.net/11375/26061
Berkhuijsen, E. M., & Fletcher, A. 2008, MNRAS, 390, L19
Bigiel, F., Leroy, A., Walter, F., et al. 2008, AJ, 136, 2846
Bigiel, F., Leroy, A. K., Blitz, L., et al. 2015, ApJ, 815, 103
Bolatto, A. D., Wolfire, M., & Leroy, A. K. 2013, ARA&A, 51, 207
Brunt, C. M., Federrath, C., & Price, D. J. 2010, MNRAS, 405, L56
Burkhart, B. 2018, ApJ, 863, 118
Burkhart, B., & Lazarian, A. 2012, ApJl, 755, L19
Burkhart, B., Lee, M.-Y., Murray, C. E., & Stanimirović, S. 2015, ApJl, 811, L28
Burkhart, B., & Mocz, P. 2019, ApJ, 879, 129
Burkhart, B., Ossenkopf, V., Lazarian, A., & Stutzki, J. 2013, ApJ, 771, 122
Burkhart, B., Stalpes, K., & Collins, D. C. 2017, ApJl, 834, L1
Chen, H., Gao, Y., Braine, J., & Gu, Q. 2015, ApJ, 810, 140
Chen, H. H.-H., Burkhart, B., Goodman, A., & Collins, D. C. 2018, ApJ, 859, 162
Chevance, M., Madden, S. C., Fischer, C., et al. 2020, MNRAS, 494, 5279
Collins, D. C., Kritsuk, A. G., Padoan, P., et al. 2012, ApJ, 750, 13
Downes, D., Solomon, P. M., & Radford, S. J. E. 1993, ApJl, 414, L13
Draine, B. 2011, Physics of the Interstellar and Intergalactic Medium (Princeton, NJ: Princeton Univ. Press)
Evans, N. J. I., Dunham, M. M., Jørgensen, J. K., et al. 2009, ApJS, 181, 321
Federrath, C., & Banerjee, S. 2015, MNRAS, 448, 3297
Federrath, C., & Klessen, R. S. 2012, ApJ, 761, 156
Federrath, C., & Klessen, R. S. 2013, ApJ, 763, 51
Gallagher, M. J., Leroy, A. K., Bigiel, F., et al. 2018, ApJ, 858, 90
Gao, Y., & Solomon, P. M. 2004a, ApJS, 152, 63
Gao, Y., & Solomon, P. M. 2004b, ApJ, 606, 271
Ginsburg, A., Koch, E., Robitaille, T., et al. 2019, radio-astro-tools/spectral-cube: Release v0.4.5, Zenodo, doi:10.5281/zenodo.3558614
Goodman, A. A., Pineda, J. E., & Schnee, S. L. 2009, ApJ, 692, 91
Grenier, I. A., Casandjian, J.-M., & Terrier, R. 2005, Sci, 307, 1292
Grudić, M. Y., Hopkins, P. F., Faucher-Giguère, C.-A., et al. 2018, MNRAS, 475, 3511
Harris, C. R., Millman, K. J., van der Walt, S. J., et al. 2020, Natur, 585, 357
Helfer, T. T., & Blitz, L. 1997a, ApJ, 478, 162
Helfer, T. T., & Blitz, L. 1997b, ApJ, 478, 233
Hennebelle, P., & Chabrier, G. 2011, ApJl, 743, L29
Heyer, M., Krawczyk, C., Duval, J., & Jackson, J. M. 2009, ApJ, 699, 1092
Hill, A. S., Benjamin, R. A., Kowal, G., et al. 2008, ApJ, 686, 363
Hunter, J. D. 2007, CSE, 9, 90
Imara, N., & Burkhart, B. 2016, ApJ, 829, 102
Jameson, K. E., Bolatto, A. D., Wolfire, M., et al. 2018, ApJ, 853, 111
Jarrett, T. H., Chester, T., Cutri, R., Schneider, S. E., & Huchra, J. P. 2003, AJ, 125, 525
Jiménez-Donaire, M. J., Bigiel, F., Leroy, A. K., et al. 2019, ApJ, 880, 127
Kainulainen, J., Beuther, H., Henning, T., & Plume, R. 2009, A&A, 508, L35

Kainulainen, J., & Federrath, C. 2017, A&A, 608, L3
Kainulainen, J., & Tan, J. C. 2013, A&A, 549, A53
Kauffmann, J., Bertoldi, F., Bourke, T. L., Evans, N. J. I., & Lee, C. W. 2008, A&A, 487, 993
Kauffmann, J., Goldsmith, P. F., Melnick, G., et al. 2017, A&A, 605, L5
Kennicutt, R. C. J., & De Los Reyes, M. A. C. 2021, ApJ, 908, 61
Krumholz, M. R. 2014, PhR, 539, 49
Krumholz, M. R., Dekel, A., & McKee, C. F. 2012, ApJ, 745, 69
Krumholz, M. R., & McKee, C. F. 2005, ApJ, 630, 250
Lada, C. J., Lada, E. A., Clemens, D. P., & Bally, J. 1994, ApJ, 429, 694
Lada, C. J., Lombardi, M., & Alves, J. F. 2010, ApJ, 724, 687
Lada, E. A., Bally, J., & Stark, A. A. 1991a, ApJ, 368, 432
Lada, E. A., Depoy, D. L., Evans, N. J. I., & Gatley, I. 1991b, ApJ, 371, 171
Langer, W. D., Velusamy, T., Pineda, J. L., Willacy, K., & Goldsmith, P. F. 2014, A&A, 561, A122
Larson, R. B. 1981, MNRAS, 194, 809
Lee, E. J., Miville-Deschênes, M.-A., & Murray, N. W. 2016, ApJ, 833, 229
Leroy, A. K., Usero, A., Schruba, A., et al. 2017a, ApJ, 835, 217
Leroy, A. K., Schinnerer, E., Hughes, A., et al. 2017b, ApJ, 846, 71
Lombardi, M., Alves, J., & Lada, C. J. 2015, A&A, 576, L1
McMullin, J. P., Waters, B., Schiebel, D., Young, W., & Golap, K. 2007, in ASP Conf. Ser. 376, Astronomical Data Analysis Software and Systems XVI, ed. R. A. Shaw, F. Hill, & D. J. Bell (San Francisco, CA: ASP), 127
Molina, F. Z., Glover, S. C. O., Federrath, C., & Klessen, R. S. 2012, MNRAS, 423, 2680
Murphy, E. J., Condon, J. J., Schinnerer, E., et al. 2011, ApJ, 737, 67
Nordlund, Å. K., & Padoan, P. 1999, in Proc. the 2nd Guillermo Haro Conf., Interstellar Turbulence, ed. J. Franco & A. Carraminana (Cambridge: Cambridge Univ. Press), 218
Onus, A., Krumholz, M. R., & Federrath, C. 2018, MNRAS, 479, 1702
Ostriker, E. C., & Shetty, R. 2011, ApJ, 731, 41
Padoan, P., Haugbølle, T., Nordlund, Å., & Frimann, S. 2017, ApJ, 840, 48
Padoan, P., Jones, B. J. T., & Nordlund, Å. P. 1997, ApJ, 474, 730
Padoan, P., & Nordlund, Å. 2011, ApJ, 730, 40
Pineda, J. L., Langer, W. D., Velusamy, T., & Goldsmith, P. F. 2013, A&A, 554, A103
Radford, S. J. E., Solomon, P. M., & Downes, D. 1991, ApJl, 368, L15
Rieke, G. H., Alonso-Herrero, A., Weiner, B. J., et al. 2009, ApJ, 692, 556
Rosolowsky, E., & Leroy, A. 2006, PASP, 118, 590
Salak, D., Nakai, N., Seta, M., & Miyamoto, Y. 2019, ApJ, 887, 143
Scalo, J., Vázquez-Semadeni, E., Chappell, D., & Passot, T. 1998, ApJ, 504, 835
Schneider, N., André, P., Könyves, V., et al. 2013, ApJl, 766, L17
Schneider, N., Csengeri, T., Klessen, R. S., et al. 2015, A&A, 578, A29
Schneider, N., Bontemps, S., Motte, F., et al. 2016, A&A, 587, A74
Semenov, V. A., Kravtsov, A. V., & Gnedin, N. Y. 2017, ApJ, 845, 133
Shirley, Y. L. 2015, PASP, 127, 299
Sun, J., Leroy, A. K., Schruba, A., et al. 2018, ApJ, 860, 172
Sun, J., Leroy, A. K., Ostriker, E. C., et al. 2020, ApJ, 892, 148
Tabatabaei, F. S., Krause, M., Fletcher, A., & Beck, R. 2008, A&A, 490, 1005
Tilanus, R. P. J., & Allen, R. J. 1993, A&A, 274, 707
Usero, A., Leroy, A. K., Walter, F., et al. 2015, AJ, 150, 115
van der Velden, E. 2020, JOSS, 5, 2004
Vazquez-Semadeni, E. 1994, ApJ, 423, 681
Virtanen, P., Gommers, R., Oliphant, T. E., et al. 2020, NatMe, 17, 261
Wada, K., & Norman, C. A. 2001, ApJ, 547, 172
Walker, D. L., Longmore, S. N., Zhang, Q., et al. 2018, MNRAS, 474, 2373
Wilson, C. D., Bemis, A. R., & Kimli, O. 2023, MNRAS, submitted
Wilson, C. D., Elmegreen, B. G., Bemis, A., & Brunetti, N. 2019, ApJ, 882, 5
Wolfire, M. G., Hollenbach, D., & McKee, C. F. 2010, ApJ, 716, 1191
Wu, J., Evans, N. J. I., Gao, Y., et al. 2005, ApJl, 635, L173
Zamora-Avilés, M., & Vázquez-Semadeni, E. 2014, ApJ, 793, 84